

Intrusion of liquids into liquid infused surfaces

with nanoscale roughness

Swarn Lata Singh^{1,2,3}, Lothar Schimmele^{1,2}, and S. Dietrich^{1,2}

¹ *Max-Planck-Institut für Intelligente Systeme,*

D-70569 Stuttgart, Heisenbergstr. 3, Germany,

² *IV. Institut für Theoretische Physik, Universität Stuttgart,*

Pfaffenwaldring 57, D-70569 Stuttgart, Germany

³ *Department of Physics, Mahila Mahavidyalaya (MMV),*

Banaras Hindu University, Varanasi, UP, 221005, India ^{*}

Abstract

We present a theoretical study of the intrusion of an ambient liquid into the pores of a nano-corrugated wall w . The pores are prefilled with a liquid lubricant which adheres to the walls of the pores more strongly than the ambient liquid does. The two liquids are modeled as a binary liquid mixture of two species of particles, A and B . The mixture can decompose into a liquid rich in A particles, representing the ambient liquid, and another one rich in B particles, representing the liquid lubricant. The wall is taken to attract the B particles more strongly than the A particles. The ratio $w\text{-}A/w\text{-}B$ of these interaction strengths is changed in order to tune the contact angle θ_{AB} formed by the A -rich/ B -rich liquid interface between the two fluids and a planar wall, composed of the same material as the one forming the pores. We use classical density functional theory, in order to capture the effects of microscopic details on the intrusion transition, which occurs as the concentration of the minority component or the pressure in the bulk of the ambient liquid is varied, moving away from bulk liquid–liquid coexistence within the single-phase domain of the A -rich bulk ambient liquid. These liquid structures have been studied as a function of the contact angle θ_{AB} and for various widths and depths of the pores. We also studied the reverse process in which a pore initially filled with the ambient liquid is refilled with the liquid lubricant. The location of the intrusion transition, with respect to its dependence on the contact angle θ_{AB} and the width of the pore, qualitatively follows the corresponding shift of the capillary-coexistence line away from the bulk liquid–liquid coexistence line, as predicted by a macroscopic capillarity model.

Quantitatively, the transition found in the microscopic approach occurs somewhat closer to the bulk liquid–liquid coexistence line than predicted by the macroscopic capillarity model. The quantitative discrepancies become larger for narrower cavities. In cases in which the wall is completely wetted by the lubricant ($\theta_{AB} = 0$) and for small contact angles the reverse transition follows the same path as for intrusion; there is no hysteresis. For larger contact angles hysteresis is observed. The width of the hysteresis increases with increasing contact angle. A reverse transition is not found inside the domain within which the ambient liquid forms a single phase in the bulk, once θ_{AB} exceeds a geometry dependent threshold value. According to the macroscopic capillarity theory, for the considered geometry, this is the case for $\theta_{AB} > 54.7^\circ$. Our computations show, however, that nanoscale effects shift this threshold value to much higher values. This shift increases strongly if the widths of the pores become smaller (below about ten times the diameter of the A and B particles).

PACS numbers: 05.20.Jj, 05.07.Np, 68.08.-p

* swarn@bhu.ac.in

I. INTRODUCTION

Super-liquid-repellent surfaces are of much interest for designing surfaces with anti-fouling, -fogging, -icing, or self-cleaning properties, for microfluidic applications, and in order to reduce drag in flow along these interfaces [1–10], to provide a few examples. Most of the synthetic liquid-repellent surfaces are inspired by the lotus effect [11], which is based on forming micro/nano structures on the surfaces. The liquid-repellency of these surfaces is due to a combination of surface chemistry, which facilitates to create a lyophobic surface, and surface roughness. This combination allows air pockets to stay within the surface roughness, which inhibit the effective contact between the liquid and the solid surface, enabling the liquid to roll off easily [12–16]. A potential problem concerning the applicability of such surfaces arises, because the trapped air pockets cannot sustain pressure and the surface loses liquid-repellency under increased pressure, e.g., as a drop of liquid impacts on the surface. Furthermore, for surfaces with micronscale roughness the liquid-repellency cannot be restored easily after a pressure induced collapse of the air pockets. By adding nanoscale roughness this problem can be avoided in principle so that robust liquid-repellent surfaces can be fabricated [17, 18]. Other problems might arise from the occurrence of surface defects and irreparable damages and contaminations which accumulated over time [2, 19–25]. The challenge of preparing robust and durable liquid-repellent surfaces increases further for liquids with low surface tension such as organic liquids [26–28].

A different route towards the development of stable liquid repellent surfaces utilizes low surface tension liquids (lubricant) infused into the surface protrusions. The lubricating liquid is chosen such that it is immiscible with the ambient liquid and has a higher affinity to the solid walls in comparison to that of the ambient liquid. Such arrangements are known as slippery liquid infused porous surfaces (SLIPS) [2, 29, 30]. It is expected that the 'incompressibility' of the lubricating liquid provides SLIPS the robustness which air pockets, being highly compressible, cannot. In addition SLIPS may exhibit other useful properties such as the ability of the lubricant to flow into damaged sites on the underlying surface and to stabilize them [2, 16]. Numerous studies have been devoted to the application of SLIPS as anti-fouling [31–33] and anti-icing [34–36] surfaces, and to surfaces which facilitate condensation and heat transport [37–39]. In addition to generally demonstrating the potential of SLIPS, most further efforts focus on novel methods of fabricating such surfaces [40–49]. However, detailed investigations of the wetting behavior of lubricant infused surfaces, as a function of various system parameters, remain sparse [9, 50, 51, 55].

The purpose of the present theoretical study is to provide an understanding of the stable and metastable thermodynamic states of lubricant infused surfaces, which are in contact with an ambient liquid. These states are investigated as functions of the interactions of the ambient liquid and of the lubricant liquid, respectively, with the solid surface. The dependence on the linear dimensions of the surface corrugations is discussed as well. In this

context, as the simplest case we consider a binary liquid mixture composed of, say, A and B particles (molecules), which decomposes into a liquid rich in A particles, representing the ambient liquid, and an other liquid rich in B particles, representing the lubricant. The lubricant adheres to the pore walls more strongly than the ambient fluid, i.e., in the present model the B particles are attracted by the walls more strongly than the A particles. The mutual solubility might be very low, but is nonzero. The concentration of the minority component in the ambient liquid (i.e., the concentration of the B particles) is varied within the single-phase domain of the A -rich bulk ambient liquid in order to find out how this variation affects the stability of the lubricant infused configuration.

We are especially interested in nanoscale effects, which become relevant if the corrugations become very narrow with linear dimensions of nanometer size. For this reason we use classical density functional theory (DFT), which captures microscopic details of the system, such as the extended range of the interactions between the liquid particles and between the liquid particles and the particles forming the solid surfaces, packing effects due to the strong repulsion between particles at short distances, and the widths of the various interfaces as well as their molecular structure. We are particularly interested in the intrusion of the ambient liquid into the lubricant infused nano-pores, triggered by variations of the composition of the ambient liquid and of its pressure. Furthermore, we study the reformation of the lubricant infused configuration from a configuration in which the pores are filled with the ambient

liquid. These processes are studied as a function of the lubricant–wall interaction strength and of the width and depth of the pores.

Our study is also relevant for designing channels and pores with sharp gating abilities. These channels, if filled with a 'gating liquid' (i.e., a lubricant) strongly wetting the pore walls, prevent passage of an ambient liquid. Upon changing conditions in the ambient liquid, the 'gating liquid' gives way and the ambient liquid can pass the channel [52, 53]. In this context selectivity and reversibility of this mechanism are important issues.

Examples of such pores are actually found in nature, such as the nuclear pore complex in eukaryotic cells and Stomata and Xylem in plants, which use liquids to mechanically reconfigure the pores [54, 56]. Another example related to our studies consists of porous surfaces the physical properties of which can be changed by switching between a state, in which the pores are filled with a lubricant, and one in which the pores are filled with an ambient liquid.

It should be noted, that in our studies transitions between thermodynamically stable or metastable states are considered. In some of the experimental studies and applications, chemical equilibrium might not be reached within the typical duration of the experiment or of the considered process. Nevertheless, also in these cases, knowledge of the equilibrium configurations is needed for a proper interpretation of the experimental results and this knowledge should also be useful in designing systems for specific applications.

In the next section (Sec. II), details of our model system are described, as well as the computational method. Furthermore, we discuss liquid–liquid coexistence in the bulk and we describe the modifications to be expected, based on macroscopic capillarity theory, if these liquids coexist within a capillary. Based on this discussion, we can make a macroscopic prediction concerning the intrusion of the ambient liquid into a lubricant infused pore. In the following sections we present and discuss the results of the microscopic DFT computations.

II. MODEL SYSTEM

In order to model a liquid infused porous surface, we consider a fluid which is composed of A and B particles. The parameters for the fluid–fluid interactions and the thermodynamic conditions are chosen such that in the bulk the fluid is in a liquid state which phase separates into an A -rich and into a B -rich liquid. In the following the A -rich liquid is denoted as L_A , the B -rich liquid as L_B . For a suitable choice of parameters, the A -rich liquid may contain up to a few percent of B particles, and vice versa the B -rich liquid contains a few percent of A particles. The porous surface is modeled by engraving square nanopits into an otherwise flat solid surface, also called a wall (see Fig. 1). The pits are periodically repeated with the periodicity length chosen to be sufficiently large such that the periodicity is irrelevant for the present investigations. The interaction strength between the B particles and the wall is taken to be stronger than the one between the A particles and the wall. Thus the B -rich

liquid L_B adheres strongly to the walls of the pits. The B -rich liquid L_B represents the lubricant whereas the A -rich liquid L_A represents an ambient liquid, which is always present above the wall and may or may not intrude into a pit initially filled with the lubricant L_B . We consider stable or metastable equilibria in a grand canonical ensemble. This implies that starting from an initial configuration the A and B particles are allowed to 'diffuse' between the ambient liquid above the wall and the liquid inside the pit until chemical equilibrium is reached. Since on the nanoscale interdiffusion is very fast, this scenario is of practical relevance. Even on larger length scales the configurations, which are stable on a longer time scale, correspond to the ones considered here. This phenomenon exhibits obvious similarities with the Cassie–Wenzel transition, which refers to the intrusion of a liquid into vapor-filled surface asperities (see, e.g., Refs. [12, 13, 15–19, 57]). In the following we shall use a corresponding terminology. The wetting state, in which the pits are completely filled with the lubricant (L_B) and the ambient liquid (L_A) remains suspended above the wall, is called the Cassie state, whereas the Wenzel state corresponds to a state in which the ambient liquid intrudes the pit and replaces the lubricant. The Cassie–Wenzel transition (i.e., the intrusion of ambient liquid L_A into a pit filled with lubricant L_B) and the reverse transition (removing the ambient liquid L_A from the pit and restoring the filling with lubricant L_B), called Wenzel–Cassie transition, is studied as a function of various system parameters. We also want to point out, that there are similarities to the filling transitions which are observed

if a wall with surface asperities is exposed to vapor and is partially filled by the coexisting liquid phase (see, e.g., Refs. [58–61]). The correspondence is less obvious in this case, due to different conditions and dependences studied in these investigations. In the following subsections the various pieces of the system, the numerical method, which is based on classical density functional theory (DFT), and that part of the bulk phase diagram, which is relevant for the present investigations, are explained in more detail.

A. Binary liquid mixture

The particles A and B forming the binary liquid mixture are considered to interact via Lennard-Jones (LJ) pair potentials. In the spirit of DFT as used here and discussed in more detail below, each pair potential is replaced by the sum of hard sphere interactions

$$U_{ij}^{hs}(r) = \begin{cases} \infty, & r \leq \sigma_{ij} = R_i + R_j, \\ 0, & r > \sigma_{ij} \end{cases} \quad (2.1)$$

and of a soft attractive part [62]

$$U_{ij}^{att}(r) = -\epsilon_{ij}\Theta(2^{1/6}\sigma_{ij} - r) + \Phi_{ij}^{LJ}(r)\Theta(r - 2^{1/6}\sigma_{ij}) \quad (2.2)$$

with the Heaviside function Θ and

$$\Phi_{ij}^{LJ} = 4\epsilon_{ij} \left[\left(\frac{\sigma_{ij}}{r} \right)^{12} - \left(\frac{\sigma_{ij}}{r} \right)^6 \right]. \quad (2.3)$$

Here, i and j represent the two species A and B of the binary liquid mixture, R_i is the radius of the fluid particles of species i , $-\epsilon_{ij}$ is the potential depth for the ij -pair potential at $r = 2^{1/6}\sigma_{ij}$, r is the center-to-center interparticle separation, and σ_{ij} is the distance of contact between the centers of two hard sphere particles. For simplicity, the binary liquid mixture is considered to be symmetric with $R_A = R_B = R$ so that $\sigma_{ij} = \sigma = 2R$ and $\epsilon_{AA} = \epsilon_{BB}$, where ϵ_{ij} is the strength of the ij -pair potential. The fluid–fluid interaction is rendered effectively short-ranged by introducing a cut-off at $r = R_{cut}$. In the following we adopt $R_{cut} = 5R$, which is implemented by a cut-off function. The interaction parameters ϵ_{ij} for the cut-off potential are rescaled such that the integrated interaction is equal to the original one resulting from the potential in Eq. (2.3) with $R_{cut} \rightarrow \infty$. For further details see Refs. [57, 63].

B. Fluid–wall interaction and wall topography

The wall is modeled as a block of solid particles C occupying a simple cubic lattice. Certain lattice sites are left unoccupied, such that a wall with the desired corrugation is

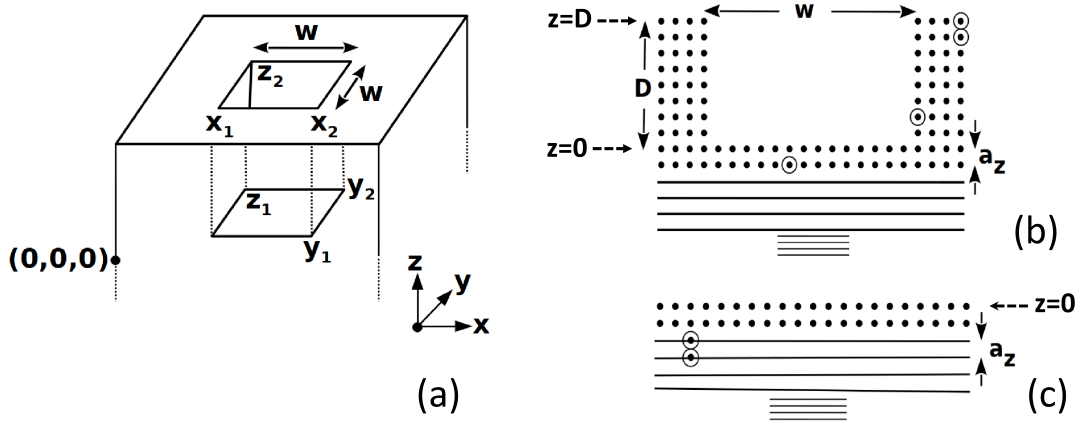


FIG. 1. (a) Schematic representation of the structured wall studied here. The structure is modeled by square pits $w \times w \times D$ of width w and depth D . The pits are carved out from a planar wall. In (a) and (b) a single pit is shown. The solid substrate is modeled as a simple cubic lattice occupied densely by particles of type C . The lattice spacing is a_z which equals twice the radius R_C of the C particles. The circles indicate the size of the C particles. In (b), the vertical cross section of the pit is shown. For lattice planes sufficiently far from the liquid volume, discrete sums (dots) are replaced by integrals (full horizontal lines), in order to speed up the calculations. In (c) the reference configuration of the planar substrate is shown, for which the surface tensions σ_{sA} and σ_{sB} (see Eq. (2.10)) between the solid substrate and the A -(B -) rich liquid are determined. The lengths w and D are measured between the respective loci of the nuclei of the C particles. These definitions imply that they encompass the corresponding depletion zone for the density profiles of the fluid particles.

formed (see Fig. 1). The solid particles C interact with the liquid particles via a Lennard-Jones potential. Summing over all interactions one obtains the wall potential acting on a fluid particle of sort i ($i = A$ or B) as

$$V_{i,ext}(\mathbf{r}) = -4\epsilon_i \sum_l \left[\left(\frac{\sigma_i}{|\mathbf{r} - \mathbf{r}_l|} \right)^{12} - \left(\frac{\sigma_i}{|\mathbf{r} - \mathbf{r}_l|} \right)^6 \right]. \quad (2.4)$$

The parameter ϵ_i defines the strength of the interaction between a solid particle C at lattice site \mathbf{r}_l and a fluid particle of sort i at \mathbf{r} , $\sigma_i = R_i + R_C = R + R_C$, and R_C is the radius of the solid particles. In Eq. (2.4) the sum over l amounts to a sum over all lattice sites

occupied by C particles. In order to speed up the computations of $V_{i,ext}$ some modifications are introduced, as described in Ref. [57]. However, these have negligible effects on $V_{i,ext}(\mathbf{r})$.

C. Classical density functional theory (DFT)

The grand canonical potential Ω of a classical system of an N -component mixture follows from the variational functional

$$\Omega[\{\rho_i\}] = F[\{\rho_i\}] + \sum_{i=1}^N \int d^3r \rho_i(\mathbf{r})(V_{i,ext}(\mathbf{r}) - \mu_i) \quad (2.5)$$

of the one-particle number densities $\rho_i(\mathbf{r}), i = 1, \dots, N$. F is the Helmholtz free energy functional, $V_{i,ext}(\mathbf{r})$ is the external potential, and μ_i is the chemical potential of species $i = A, B$, respectively. The equilibrium number densities $\rho_{i,0}(\mathbf{r})$ minimize Ω :

$$\left. \frac{\delta \Omega[\rho_i]}{\delta \rho_i(\mathbf{r})} \right|_{\rho_i(\mathbf{r})=\rho_{i,0}(\mathbf{r})} = 0. \quad (2.6)$$

$\Omega[\{\rho_{i,0}\}]$ is the equilibrium grand canonical potential of the system [64, 65]. The free energy functional can be divided into two parts:

$$F[\{\rho_i\}] = F_{id}[\{\rho_i\}] + F_{ex}[\{\rho_i\}], \quad (2.7)$$

where F_{id} is the ideal gas part

$$F_{id}[\rho_i] = k_B T \sum_{i=1}^N \int d^3r \rho_i(\mathbf{r}) [\ln(\rho_i(\mathbf{r})\Lambda_i) - 1], \quad (2.8)$$

$\Lambda_i = (\frac{h^2}{2\pi m_i k_B T})^{3/2}$ is the cube of the thermal wavelength associated with a particle of species i and mass m_i , h is Planck's constant, and k_B is the Boltzmann constant. The excess part F_{ex} arises due to the interparticle interactions. We approximate the excess part as the sum of two distinct contributions: one arising due to the hard core repulsion (F_{hs}), and the other due to the attractive part of the interaction (F_{att}):

$$F_{ex} = F_{hs} + F_{att}. \quad (2.9)$$

F_{hs} is treated within the framework of fundamental measure theory (FMT), as described in, e.g., Refs. [57, 63, 66–68]; we have chosen the variant proposed by Rosenfeld *et al.* [69].

F_{att} is approximated within a simple random phase approximation. In order to approximate F_{att} , we have used the following truncation of the corresponding functional perturbation expansion:

$$F_{att} = \frac{1}{2} \sum_{i,j=1}^N \int d^3r \int d^3r' \rho_i(\mathbf{r}) \rho_j(\mathbf{r}') U_{ij}^{att}(\mathbf{r} - \mathbf{r}')$$

with U_{ij}^{att} defined via Eqs. (2.2) and (2.3). Here, the minimization of $\Omega[\{\rho_i\}]$ has to be carried out numerically. The number density is discretized on a simple cubic grid, and a Picard iteration scheme is used in order to minimize Ω and to determine the equilibrium number densities. Details about the computational techniques can be found in Refs. [57, 63, 70].

D. Bulk liquid–liquid coexistence

In what follows we study, as already mentioned, a symmetric binary liquid mixture, i.e., the radii of the A and the B particles are equal ($R_A = R_B = R$) and the strengths of the A – A and B – B interactions are equal, too, i.e., $\epsilon_{AA} = \epsilon_{BB}$. We further fix the temperature such that $T = 0.899\epsilon_{AA}/k_B$. The strength of the A – B interaction relative to the A – A (B – B) interaction is fixed to the value $\epsilon_{AB}/\epsilon_{AA} = 0.77$. The parameters are chosen such that thermodynamically the fluid is away from criticality and also from solidification. Moreover the parameters are selected such that the liquid is demixed. Otherwise, the choice of the precise numbers is rather arbitrary. In addition to the number densities ρ_A and ρ_B of the A and B particles, respectively, we also introduce the concentrations $c_A = \rho_A/(\rho_A + \rho_B)$ and $c_B = \rho_B/(\rho_A + \rho_B)$ (with $c_B = 1 - c_A$), as well as the total fluid packing fraction $\eta = \eta_A + \eta_B$ with $\eta_A = (4\pi/3)R_A^3\rho_A$ and $\eta_B = (4\pi/3)R_B^3\rho_B$; η_A and η_B are the fluid volume fractions blocked by the hard cores of the A and B fluid particles, respectively. A cut through the bulk phase diagram of this liquid at the temperature $T = 0.899\epsilon_{AA}/k_B$, as computed by

using the DFT version described above, is shown in Fig. 2 in a plane spanned by the variables c_A and η . The cyan line gives the concentration c_A and the total packing fraction η of the A -rich liquid L_A at coexistence with the B -rich liquid L_B , the c_A and η values of which are defined by the blue line; the two coexisting liquids always have the same η values. For completeness we also show as red lines the c_A and η values for the liquids L_A and L_B , respectively, at coexistence with vapor, the c_A and η values of which are defined by the right edge of the brownish stripe at small total packing fraction η . The liquids, in general, have concentrations c_A , which are very different from the ones of the coexisting vapor. When the red lines meet the cyan and blue lines, one has three-phase coexistence between the two liquids L_A and L_B , and the vapor with concentration $c_A = 0.5$. Upon varying temperature the three-phase coexistence points form the triple line of binary liquid mixtures.

In the following studies of the Cassie–Wenzel or Wenzel–Cassie transitions the concentration c_A and the total packing fraction η in the ambient liquid L_A are controlled. The changes of parameters create the vertical path P_1 (variation of c_A at fixed η) or the horizontal path P_2 (variation of η at fixed c_A), as indicated in the inset of Fig. 2.

E. Macroscopic theory of liquid–liquid coexistence in a capillary

If the liquid is confined between macroscopically extended walls, the liquid–liquid coexistence lines are shifted. The size and the direction of this shift depend also on the fluid–wall

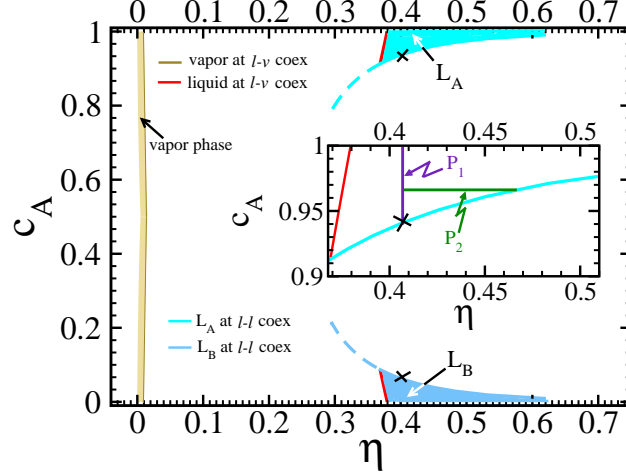


FIG. 2. Cut through the bulk phase diagram of the symmetric binary liquid, which is composed of A and B particles ($\epsilon_{AA} = \epsilon_{BB}$, $\epsilon_{AB} = 0.77\epsilon_{AA}$, $R_A = R_B = R$), at fixed temperature $T = 0.899\epsilon_{AA}/k_B$; c_A is the concentration of A particles and $\eta = \eta_A + \eta_B$ is the total packing fraction. The right edge of the brownish stripe, at low η , represents the c_A and η values of the vapor coexisting with an A -rich liquid (L_A) or B -rich liquid (L_B); the red lines represent the respective c_A and η values of the coexisting liquids. The cyan line defines the c_A and η values of the liquid L_A at coexistence with the liquid L_B ; the c_A and η values for L_B at liquid-liquid coexistence is represented by the blue line. In the studies of the Cassie-Wenzel transition, c_A and η in the ambient liquid L_A are controlled. L_A (L_B) is the stable liquid for concentrations c_A above (below) the cyan (blue) line. The dashed lines extend the liquid-liquid coexistence lines into the range within which liquid is only metastable. The crosses on the liquid-liquid coexistence lines mark the pair of reference points used in the linearization described in Sect. II E. In the inset P_1 and P_2 indicate two thermodynamic paths (see the main text).

interactions. In order to study these shifts we first consider predictions based on the macroscopic capillarity theory. In order to facilitate comparisons with the full DFT calculations, the corresponding macroscopic parameters are computed by using DFT. In this context, the most important macroscopic parameter is the contact angle θ_{AB} , at which the L_A - L_B interface meets the surface of a solid wall (see Fig. 3). The contact angle θ_{AB} follows from

Young's law

$$\cos \theta_{AB} = \frac{\sigma_{sA} - \sigma_{sB}}{\sigma_{AB}}, \quad (2.10)$$

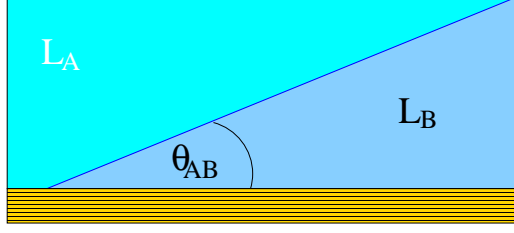


FIG. 3. The L_A – L_B interface and the surface of the solid wall form the contact angle θ_{AB} (see Eq. (2.10)).

where σ_{sA} , σ_{sB} , and σ_{AB} are the interfacial tensions of the solid– L_A , the solid– L_B , and the L_A – L_B interface, respectively; σ_{AB} and thus θ_{AB} are properly defined only at bulk L_A – L_B coexistence, but not for complete wetting [71].

At bulk L_A – L_B coexistence the following three conditions hold:

$$\mu_A^{L_B}(c_A^{L_B,co}, \eta^{L_B,co}) = \mu_A^{L_A}(c_A^{L_A,co}, \eta^{L_A,co}); \quad \mu_B^{L_B}(c_A^{L_B,co}, \eta^{L_B,co}) = \mu_B^{L_A}(c_A^{L_A,co}, \eta^{L_A,co}); \quad p^{L_B} = p^{L_A}. \quad (2.11)$$

Here, $\mu_i^{L_B}$ and $\mu_i^{L_A}$ are the chemical potentials of species i in the liquid L_B and L_A , respectively. The concentrations of A particles in the coexisting liquids L_B and L_A , respectively, are denoted as $c_A^{L_B,co}$ and $c_A^{L_A,co}$ (with $c_B = 1 - c_A$); the corresponding total packing fractions are $\eta^{L_B,co}$ and $\eta^{L_A,co}$, respectively. The pressures p in the two liquids are equal. However, in confinement the pressures of the two coexisting liquids are no longer equal. Within the macroscopic capillary theory, the grand potential can be expressed in terms of volume and interfacial contributions. Equating the grand potentials for a large but finite capillary with square cross section (see Fig. 1), which is filled with either liquid L_A or liquid L_B , one

obtains

$$p^{L_A} - p^{L_B} = \frac{4(\sigma_{sA} - \sigma_{sB})}{w}, \quad (2.12)$$

which replaces the last equation in Eq. (2.11). According to Eq. (2.10) and with $(\sigma_{sA} - \sigma_{sB})/\sigma_{AB} \in [1, -1]$, Eq. (2.12) can be expressed as

$$p^{L_A} - p^{L_B} = \frac{4\sigma_{AB} \cos \theta_{AB}}{w}. \quad (2.13)$$

The change of the pressure conditions, from equal pressure in the two liquids at bulk coexistence to a pressure difference as given by Eq. (2.12) in the two coexisting liquids confined by a capillary, leads to a shift of the coexistence lines for capillary coexistence away from the bulk coexistence lines. This shift can be approximately determined by linearizing the pressure and the chemical potentials for both species, as a function of concentration and total packing fraction, about a pair of reference points on the bulk coexistence lines. Such a pair of coexisting liquids L_A and L_B is indicated by the two crosses on the coexistence lines in Fig. 2. This linear expansion is given by

$$p^{L_A} = p^{ref} + \frac{\partial p}{\partial c_A}|_{ref,A} \Delta c_A^{L_A} + \frac{\partial p}{\partial \eta}|_{ref,A} \Delta \eta^{L_A}, \quad (2.14)$$

$$p^{L_B} = p^{ref} + \frac{\partial p}{\partial c_A}|_{ref,B} \Delta c_A^{L_B} + \frac{\partial p}{\partial \eta}|_{ref,B} \Delta \eta^{L_B},$$

and similarly for $\mu_A^{L_A}$, $\mu_A^{L_B}$, $\mu_B^{L_A}$, and $\mu_B^{L_B}$.

In Eq. (2.14) p^{ref} is the coexistence pressure of the liquids L_A and L_B at the chosen reference points; $(\Delta c_A^{L_A}, \Delta \eta^{L_A})$ and $(\Delta c_A^{L_B}, \Delta \eta^{L_B})$ are the deviations of the concentration and the packing fraction from their reference values for the A -rich and the B -rich liquid, respectively. The derivatives are taken at the reference points on the A -rich and the B -rich side, indicated as $|_{ref,A}$ and $|_{ref,B}$, respectively. Inserting these linear expansions (Eq. (2.14)) into the conditions for capillary coexistence, i.e., the equality of the chemical potentials in the A -rich and the B -rich liquid of both species (the first two of Eqs. (2.11)) and the pressure condition (Eq. (2.12)), leads to three linear equations. We are mainly interested in the shift $\Delta c_A^{L_A}$ of the capillary coexistence line of the A -rich liquid at a given packing fraction; in the following, the concentration and total packing fraction in the A -rich liquid are prescribed and fix the chemical potentials of both species. Solving the system of linear equations for $\Delta \eta^{L_A} = 0$ (the total packing fraction in the A -rich liquid is fixed and equal to the reference value) we find

$$\Delta c_A^{L_A} = \frac{\sigma_{AB} \cos \theta_{AB}}{w} f(T, \eta_{ref}) \quad \text{or} \quad \Delta c_A^{L_A} = \frac{\sigma_{sA} - \sigma_{sB}}{w} f(T, \eta_{ref}); \quad (2.15)$$

the function $f(T, \eta_{ref})$ depends only on bulk fluid properties, not on the wall properties, and not on the geometry. (Capillary coexistence of two liquids is discussed also in Ref. [72].)

For $\theta_{AB} = 0^\circ$ (complete wetting), the macroscopic estimate (Eq. (2.15)) for capillary coexistence is no longer based on solid ground. In this case the equilibrium structure of a

wall- L_A interface involves a macroscopic film of L_B between the liquid L_A and the wall. The equilibrium surface tension of this composite interface is thus the sum of the wall- L_B surface tension and of the L_B - L_A surface tension ($\sigma_{sA} = \sigma_{sB} + \sigma_{AB}$, which implies $(\sigma_{sA} - \sigma_{sB})/\sigma_{AB} = 1$; see below). However, in deriving Eq. (2.15) two configurations are compared, one of which is a capillary filled with the L_A liquid. A surface tension involving a macroscopic L_B film is not useful for computing the surface contribution to the free energy of such a configuration, because having a thick L_B film does not leave space for a L_A liquid in a nanoscopic capillary. In this context one should also note that capillary coexistence, for the interaction strengths considered here, is shifted into the L_A single-phase domain. For this thermodynamic condition the wall- L_A interface structure contains only a microscopically thin ' L_B film'. In this case the surface contribution to the free energy is obtained by replacing the equilibrium surface tension σ_{sA} by the 'surface tension' of a configuration without a macroscopically thick wetting film. At bulk liquid-liquid coexistence this non-equilibrium 'surface tension' might be inferred from a constrained minimization of the variational free energy functional. With this non-equilibrium 'surface tension' ' σ'_{sA} ' we can define the ratio $(\sigma'_{sA} - \sigma_{sB})/\sigma_{AB}$, which now becomes larger than 1, because ' σ'_{sA} ' must be larger than the equilibrium value. The macroscopic estimate for capillary coexistence, in the case of complete wetting, should be based on Eq. (2.15), but replacing $\cos\theta_{AB} = 1$ by $(\sigma'_{sA} - \sigma_{sB})/\sigma_{AB} > 1$. We have refrained from carrying out the required constrained

minimizations. Instead, in the case of complete wetting, we only give a lower bound to the macroscopic estimate for the concentration c_A^{LA} for capillary coexistence, which follows from Eq. (2.15) with $\cos \theta_{AB} = 1$.

For $\theta_{AB} < 90^\circ$, the capillary coexistence line shifts towards higher concentrations c_A^{LA} of A particles in the A -rich liquid. We now consider this case and study the force balance at the interface between the liquid L_A , which fills, say, the upper part of the capillary shown in Figs. 1 (a) and (b), and the liquid L_B , which fills the lower part. The capillary forces, due to the interfacial tensions, tend to drive the A -rich liquid out of the capillary. These forces can be balanced by the pressure force, provided the pressure in the A -rich liquid L_A is higher than it is in the B -rich liquid L_B (see the pressure condition in Eq. (2.12)). Now we monitor the system if one moves in the phase diagram along path P_1 (see Fig. 2), starting at the bulk coexistence line and then enhancing the concentration c_A^{LA} towards capillary coexistence at $c_A^{LA} + \Delta c_A^{LA}$ (not shown in Fig. 2). Figure 4 shows that the pressure in the L_A liquid decreases as one moves towards higher c_A^{LA} . However, in order to maintain chemical equilibrium the concentration and the total packing fraction in the L_B liquid move away from their values at bulk coexistence such that the pressure in the B -rich liquid drops even more than it does in the A -rich liquid. At capillary coexistence, which is reached at the concentration $c_A^{LA,co} + \Delta c_A^{LA}$ (see Eq. (2.15)), the pressure difference reaches the value required for a balance of pressure and capillary forces. At higher values of c_A^{LA} the pressure

in the liquid L_B becomes too low, the position of the interface becomes unstable, and moves downwards (see Fig. 1), expelling the liquid L_B from the capillary. In the case that $c_A^{L_A}$ is below its capillary-coexistence value $c_A^{L_A,co} + \Delta c_A^{L_A}$, the position of the interface is unstable, too, but now the liquid L_A is expelled from the capillary.

Based on this picture we can describe the intrusion of the liquid L_A into a pit initially filled with the liquid L_B . Within a macroscopic description, the force balance at the L_A – L_B interface is the same for all positions of the interface between the upper opening of the pit (Fig. 1) and a position just above the pit floor. Therefore, on the level of a macroscopic description it is predicted, that the liquid L_A abruptly intrudes the pit once $c_A^{L_A}$ is increased above the capillary-coexistence value $c_A^{L_A,co} + \Delta c_A^{L_A}$.

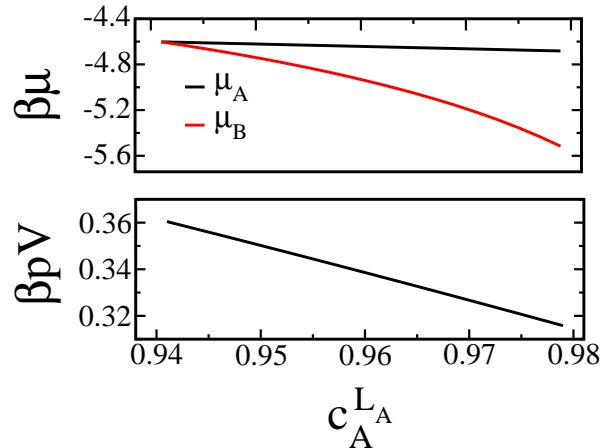


FIG. 4. Variation of the chemical potentials μ_A and μ_B of the two species and of the pressure in the A -rich liquid L_A along path P_1 (see Fig. 2); $V = R^3$ and $\beta = 1/(k_B T)$. At liquid–liquid coexistence μ_A and μ_B are equal due to the A – B symmetry

F. Computational details

In all computations discussed below, the relative strength of the A - B to the A - A (B - B) interaction has been fixed to the value $\epsilon_{AB}/\epsilon_{AA} = 0.77$. Furthermore the temperature is fixed to $T = 0.899\epsilon_{AA}/k_B$. These are the values used in Fig. 2. The wall- A interaction (ϵ_A) is fixed as well, and it is chosen such that a pure A liquid, at liquid-vapor coexistence, forms a contact angle of $\approx 157^\circ$ with the corresponding planar wall surface. The wall- B interaction (ϵ_B) is varied, and it is quantified in terms of the contact angle θ_{AB} shown in Fig. 3; θ_{AB} is computed from Young's law (Eq. (2.10)).

In the following we present our results of the full DFT computations. In these studies we determine the conditions under which the A -rich ambient liquid L_A intrudes into the pits filled with the B -rich lubricant L_B . The reverse transitions are studied as well. The DFT computations require the numerical minimization of the grand canonical potential $\Omega[\{\rho_i\}]$ with respect to the two number densities. The number densities are discretized on a simple cubic grid, and a Picard iteration scheme is used in order to reach the minimum of Ω and to determine the equilibrium number densities of the two species. The calculations have been carried out in a rectangular computational box. A corrugated wall containing one pit with a square cross section is placed at the bottom of the computational box with the outward normal of the wall pointing into the z -direction (see Fig. 1). The radius of the wall particles has been chosen as $R_C = R_A/3$. This choice of the size of the wall particles turns out

to be a sound compromise between minimizing the effect of wall roughness on interfacial structures and the computational cost. Periodic boundary conditions have been applied in the x - and y - directions. At the upper end of the computational box, boundary conditions are prescribed for the number densities ρ_A and ρ_B corresponding to the specified bulk A -rich liquid L_A . Due to the periodic boundary conditions in x - and y - directions, effectively a wall with a periodic array of pits is analyzed. However, the lateral dimensions of the box are chosen such that the distance between the pits is sufficiently large and the walls separating them are sufficiently thick such that effectively intrusion (extrusion) of the ambient liquid into (out of) isolated lubricant infused pits is studied. The size of the box in z -direction is also taken sufficiently large such that the bulk densities are attained near the upper end of the computational box.

In what follows, we always control the concentrations and the total packing fraction in the A -rich ambient liquid L_A , moving along the paths P_1 and P_2 indicated in Fig. 2. The properties of the B -rich liquid L_B inside the pit adjust to the thermodynamic conditions prescribed by the ambient liquid. The Cassie to Wenzel and Wenzel to Cassie transitions are studied as a function of θ_{AB} and for various widths and depths of the pits. In order to study hysteresis we carried out two sets of calculations in each case. In the first set, the iterative determination of the number densities is initialized with a distribution of number densities similar to the Cassie state. The pit is initially filled with the homogeneous B -rich

lubricant L_B ; the densities correspond to the bulk state, $\eta_{L_B} = 0.4069093$, $c_B^{L_B} = 0.941$, and $c_A^{L_B} = 0.059$, marked by a cross on the blue coexistence line in Fig. 2. Above the pit the initial densities correspond to the ambient A -rich bulk liquid L_A with the proper concentrations and total packing fraction. In the following, calculations initialized in this way are denoted as I:C (initialized: Cassie). In the second set of calculations initial conditions are chosen which correspond to the Wenzel state. In this case, the initial densities correspond to the ambient A -rich bulk liquid L_A not only above the wall surface but also inside the pit. The corresponding calculations are denoted as I:W (initialized: Wenzel).

III. RESULTS AND DISCUSSION

In order to quantify the extent of the intrusion/extrusion transitions, we have calculated the average densities of both species inside the pit volume V_p , defined as

$$\bar{\rho}_{A/B} = \frac{1}{V_p} \int_{V_p} d^3r \rho_{A/B}(\mathbf{r}) \approx \frac{1}{N} \sum_i \rho_{A/B}(x_i, y_i, z_i), \quad (3.1)$$

where i indicates a point on the discretization grid inside the pit ($x_1 \leq x_i \leq x_2$, $y_1 \leq y_i \leq y_2$, $0 \leq z_i \leq D$ (see Fig. 1)) and N is the total number of grid points inside the pit. This definition takes into account also the vanishing density within the depletion zones adjacent to the inner walls of the pits.

An alternative representation for the degree of intrusion is given by the position of the L_A - L_B interface on the four-fold symmetry axis along the z direction, passing through the centers of the square cross sections of the pit. The location of the interface is defined as the position z_{cr} where $\rho_A(z)$ and $\rho_B(z)$ cross, i.e., attain the same value. The distance z is measured from the bottom wall of the pit.

A. Cassie–Wenzel/Wenzel–Cassie transition at fixed total packing fraction

In the following the results of the full DFT computations along path P_1 (see Fig. 2) are presented. There, the concentration $c_A^{L_A}$ is varied at a fixed total packing fraction $\eta^{L_A} = 0.4069093$. According to Eq. (2.15) the shift of the concentration at capillary coexistence, away from the bulk coexistence line, is therefore computed based on the two reference points $(\eta^{L_A} = 0.4069093, c_A^{L_A} = 0.941)$ [$c_B^{L_A} = 1 - c_A^{L_A} = 0.059$] and $(\eta^{L_B} = \eta^{L_A} = 0.4069093, c_A^{L_B} = 0.059)$ [$c_B^{L_B} = 1 - c_A^{L_B} = 0.941$]. These points are marked by the two crosses on the phase boundaries shown in Fig. 2. In order to compute the shift of the concentration at capillary coexistence (based on Eq. (2.15)) via macroscopic capillary theory, the macroscopic parameters entering into it are determined by using exactly the same DFT as for the full DFT computations. The pertinent quantities follow from the equations of state for the two bulk liquids (i.e., homogeneous densities). The interfacial tensions and Young’s contact angle θ_{AB} are determined from DFT computations for systems with planar interfaces. The

locations and the nature of the transitions, observed within the full DFT computations, are compared with the ones predicted by the macroscopic theory. The latter predicts an abrupt intrusion at the shifted coexistence concentration.

1. *Dependence on the contact angle θ_{AB}*

We have fixed the pit dimensions at $w = 10\sigma$ and $D = 8\sigma$. The ratio ϵ_B/ϵ_A (Eq. (2.4)) is varied in order to change the contact angle θ_{AB} , which is computed by using Young's law $\cos \theta_{AB} = (\sigma_{sA} - \sigma_{sB})/\sigma_{AB}$. First, we choose $\epsilon_B/\epsilon_A = 4$, which corresponds to a scenario in which, at L_A - L_B coexistence in the bulk (i.e., for $c_A^{L_A} = 0.941$), the B -rich liquid wets a planar wall completely. In Fig. 5 we present the corresponding number densities of the A and B species. A thick wetting layer of the B -rich liquid L_B is observed above the wall. Of course, the configuration shown cannot correspond to a fully converged iteration; the equilibrium thickness of the wetting layer should be macroscopically thick at coexistence in the bulk. However, increasing the thickness of the wetting layer beyond the one shown, lowers the free energy barely. Because of the very slow convergence of the iteration with respect to the one particular, collective coordinate, which describes the increase of the wetting layer thickness, the densities shown in the figure virtually are the equilibrium densities for a constrained position of the L_B - L_A interface (i.e., a constrained thickness of the wetting layer). The pit is filled with the B -rich liquid L_B . Increasing the concentration $c_A^{L_A}$ of A

particles in the ambient liquid L_A to values away from coexistence (see the cyan line in Fig. 2, moving along path P_1 in Fig. 2), a gradual intrusion of the ambient liquid L_A into the pit is observed. Typical equilibrium number density distributions are shown in Fig. 6. One observes that once the concentration of A particles is increased to $c_A^{LA} = 0.967$ (Fig. 6 (d)) the lubricant L_B is replaced inside the pit completely by the ambient liquid L_A . However, because the wall attracts the B particles much stronger than the A particles, a thin B rich layer remains at the surfaces of the walls (see Fig. 6). For this choice of parameters there is no hysteresis; the equilibrium number densities are found to be independent of whether the numerical iterations are initialized in a Cassie type or in a Wenzel type configuration. The average number densities of the A and the B particles inside the pit as well as the position z_{cr} of the interface as a function of c_A^{LA} are shown in Fig. 7. These curves show a gradual decrease of the average number density of B type particles (and an increase of the average number density of A type particles) inside the pit and an interface gradually moving downwards; the strong increase of z_{cr} (panel (b) in Fig. 7) at liquid–liquid coexistence is due to the formation of the wetting layer with L_B . For comparison, in Fig. 7 the lower bound to the sharp transition, predicted by the macroscopic theory at a concentration corresponding to capillary coexistence (see Eq. (2.15) with $\cos \theta_{AB} = 1$) is indicated as a dashed vertical line in the figure.

We carried out the same type of computation as described above, by decreasing the ratio

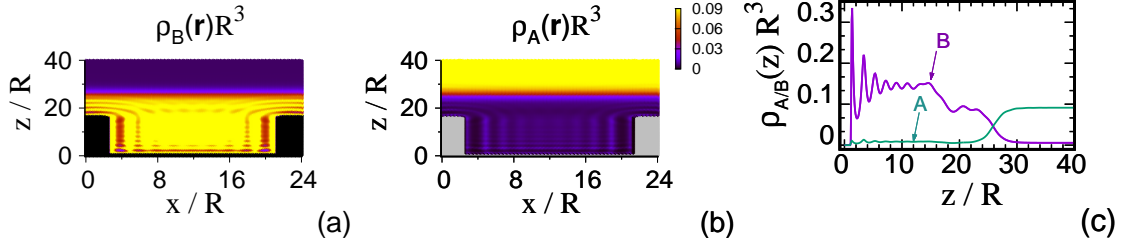


FIG. 5. Equilibrium number density distributions $\rho_B(\mathbf{r})$ (a) and $\rho_A(\mathbf{r})$ (b), at liquid–liquid coexistence ($\eta^{LA} = \eta^{LB} = 0.4069093$, $c_A^{LA} = c_B^{LB} \approx 0.941$), in the xz plane passing through the middle of the pit. The color bar applies to both (a) and (b). In (b) the regions of zero densities inside the wall and in the depletion zones are shown in gray, in order to enhance the contrast. The ratio of the wall–A and the wall–B interaction strengths is $\epsilon_B/\epsilon_A = 4$, which corresponds to complete wetting of the wall by the B-rich liquid L_B . Above the wall the A-rich liquid L_A is found, as revealed by the high number density $\rho_A(\mathbf{r})$ and the low number density $\rho_B(\mathbf{r})$ for large z . For the complete wetting scenario shown here, in reality the L_B wetting layer above the wall is macroscopically thick. The depth of the pit is $16R = 8\sigma$, and its width is $20R = 10\sigma$. Panel (c) shows the densities along the symmetry axis parallel to z , through the centers of the square cross sections. The interface position is chosen to be located at the crossing z_{cr} of $\rho_A(z)$ and $\rho_B(z)$. The remaining parameters in this and all following figures are $\epsilon_{AA}/(k_B T) = 1.112$ ($\epsilon_{BB} = \epsilon_{AA}$), $\epsilon_{AB} = 0.77\epsilon_{AA}$, and ϵ_A is chosen such that for a pure A type liquid (given the above value of $\epsilon_{AA}/(k_B T)$) the contact angle formed by its liquid–vapor interface is $\theta_Y \approx 157^\circ$.

ϵ_B/ϵ_A step by step. In this way we change from a regime, in which the B-rich liquid wets the wall completely, towards and into the regime of partial wetting, in the case of which an L_A – L_B interface meets the planar wall at a nonzero contact angle θ_{AB} . Down to a ratio $\epsilon_B/\epsilon_A = 3.5$ we do not observe a pronounced jump in the averaged number densities $\bar{\rho}_{A/B}$ or in the position z_{cr} of the L_A – L_B interface as the concentration c_A^{LA} is varied in steps of 0.001. The transition seems to be continuous although it becomes steeper and the interval, within which the steep changes occur, becomes narrower as the ratio ϵ_B/ϵ_A becomes smaller. Down to $\epsilon_B/\epsilon_A = 3.2$, corresponding to $\theta_{AB} = 12^\circ$, no hysteresis is observed, i.e., irrespective of whether the calculations are initialized in a Cassie type configuration (I:C) or in a Wenzel type configuration (I:W), the same equilibrium number densities are

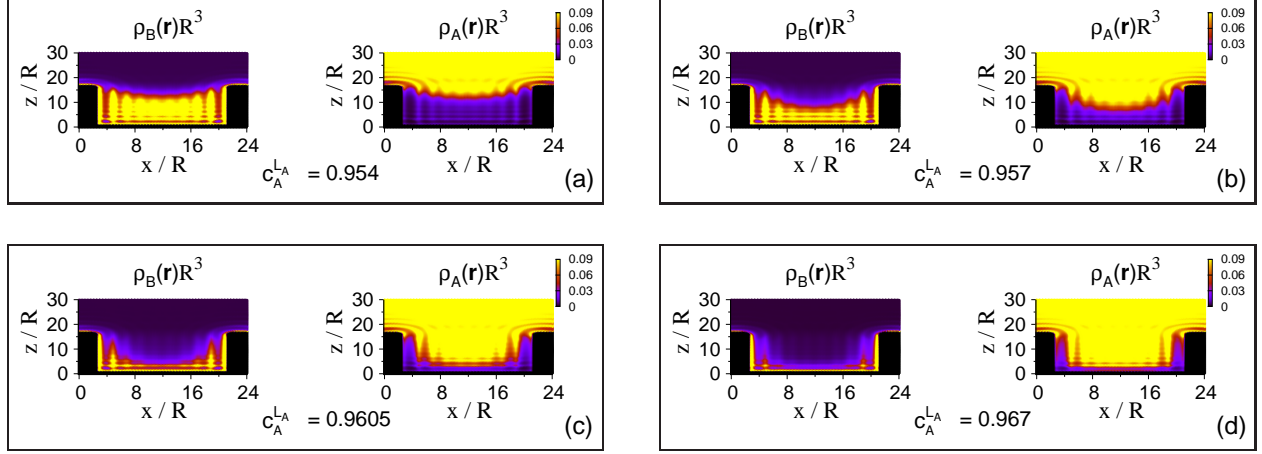


FIG. 6. Evolution of the system, which is shown in Fig. 5 at liquid–liquid coexistence, as the concentration of A particles in the ambient liquid L_A is increased at constant total packing fraction along path P_1 in Fig. 2. Here, the equilibrium number densities are independent of whether the numerical iterations are initialized in a Cassie type or in a Wenzel type configuration, as anticipated.

obtained. A small hysteresis emerges first, if ϵ_B/ϵ_A is reduced to the value 3.1. Starting in the Cassie configuration, the L_A liquid intrudes the pit for $0.953 < c_A^{L_A} < 0.954$ (the interval is defined by the steps in which the concentration is varied), whereas starting in the Wenzel configuration the Cassie configuration is restored for $0.952 < c_A^{L_A} < 0.953$, i.e., one has to move closer to the liquid–liquid coexistence line by the amount $\Delta c_A^{L_A} = 0.001$ in order to recover the Cassie state in which a pit is filled with the liquid L_B . A number of computations have been carried out for several smaller ratios ϵ_B/ϵ_A ; the smallest ratio considered has been $\epsilon_B/\epsilon_A = 2.0$, corresponding to a contact angle $\theta_{AB} = 59^\circ$. In general, the hysteresis increases with decreasing ϵ_B/ϵ_A , whereas the value of $c_A^{L_A}$, at which intrusion of the ambient liquid occurs, decreases, i.e., the transition from the Cassie to the Wenzel

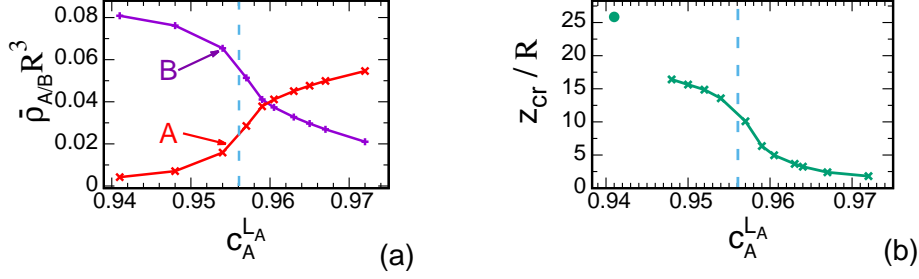


FIG. 7. Averaged number densities $\bar{\rho}_{A/B}$ of the A and the B particles inside the pit (Eq. (3.1), (a)) and the position z_{cr} of the L_A – L_B interface (panel (b)) as the concentration $c_A^{L_A}$ of A particles in the ambient liquid is varied along path P_1 in Fig. 2. The system parameters are the same as the ones for Fig. 5. Due to complete wetting at bulk liquid–liquid coexistence, one observes at the coexistence concentration $c_A^{L_A} \approx 0.941$ a large value of z_{cr} , representing an interface at a macroscopic distance above the wall (marked by a dot in panel (b)). At the next higher value of $c_A^{L_A}$ which has been investigated, z_{cr} jumps to a much smaller value, which corresponds to an interface position at the pit entrance. As $c_A^{L_A}$ is increased further, the interface gradually moves down towards the bottom of the pit (panel (b)). There is a gradual transition of the averaged number densities $\bar{\rho}_{A/B}$ of the A and the B particles inside the pit (panel (a)). No hysteresis has been observed. The number density profiles shown in Figs. 5 and 6 are in line with the transition shown here. The dashed vertical line indicates the lower bound to the macroscopic prediction for capillary coexistence of L_A and L_B , for which an abrupt intrusion of L_A into the pit occurs (Eq. (2.15) with $\cos \theta_{AB} = 1$).

state occurs closer to the bulk liquid–liquid coexistence line. Qualitatively, the shift of the intrusion concentration as observed within the full DFT computations agrees with the shift of the capillary coexistence as predicted by the macroscopic theory. The numbers, characterizing quantitatively the findings from the full DFT computations, are tabulated in

Table I together with the macroscopic predictions for the intrusion concentrations. A more detailed discussion of the DFT results is given below for three selected contact angles θ_{AB} .

The first example which we discuss corresponds to $\epsilon_B/\epsilon_A = 2.8$ (i.e., $\theta_{AB} \approx 30^\circ$). If the iterative determination of the equilibrium number densities is initialized in the Cassie state, and one then increases the concentration c_A^{LA} starting from its value at the bulk coexistence line step by step, an abrupt intrusion, i.e., an abrupt transition to the Wenzel state, is observed between $c_A^{LA} \approx 0.951$ and $c_A^{LA} \approx 0.952$ (see Fig. 8). Instead, initializing the iteration in the Wenzel state and following the results if c_A^{LA} is lowered, one finds that the system remains in the Wenzel state down to $c_A^{LA} = 0.950$. The system jumps to the Cassie state once the concentration of the A particles in the ambient liquid is reduced a tiny bit further to $c_A^{LA} = 0.949$. This means, that the Wenzel state becomes unstable in the interval $0.949 < c_A^{LA} < 0.950$, i.e. there is a small hysteresis.

In Fig. 9 we show the average number densities of the A and the B particles inside the pit as well as the position z_{cr} of the interface between the A and the B rich liquids as a function of c_A^{LA} for two different initializations of the iterations, i.e., in the Cassie state (I:C) or in the Wenzel state (I:W). Within a certain interval of the concentration c_A^{LA} , the results do depend on the initial condition. (It turns out that whether in the computations c_A^{LA} is increased or decreased is of no consequence; only the initial condition matters.) The system will go through a full hysteresis cycle, if it is initialized, e.g., in the Cassie state (i.e., the

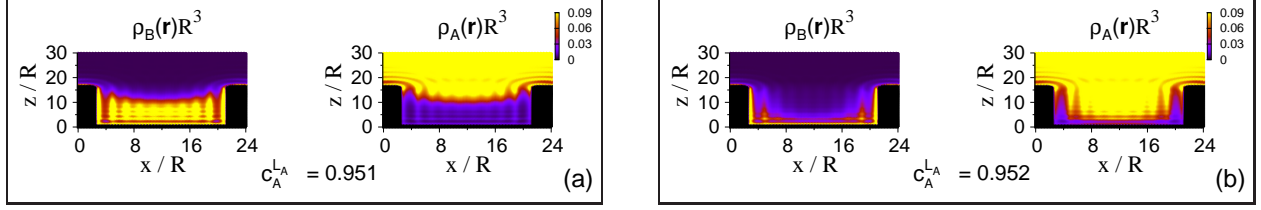


FIG. 8. Equilibrium number densities $\rho_B(\mathbf{r})$ and $\rho_A(\mathbf{r})$ in the xz plane passing through the middle of the pit for a ratio of the wall- A to the wall- B interaction strengths which corresponds to a contact angle $\theta_{AB} \approx 30^\circ$. Here, the numerical iterations are initialized in a Cassie state, i.e., the pits are initially filled with the lubricant L_B . The total packing fraction in the ambient liquid is fixed to $\eta^{L_A} = 0.4069093$, i.e., its value along path P_1 in Fig. 2. In panel (a) the concentration of A particles in the ambient liquid L_A is $c_A^{L_A} \approx 0.951$, whereas in panel (b) one has $c_A^{L_A} \approx 0.952$. Between these two concentrations an abrupt intrusion by the ambient liquid L_A is observed. The width of the pit is $20R = 10\sigma$ and the depth is $16R = 8\sigma$. The remaining parameters are the same as in all other figures.

pit is filled with the lubricant L_B) and if the A concentration $c_A^{L_A}$ in the ambient liquid is increased until the ambient liquid intrudes. In the above process the curves marked as I:C represent the state of the system. For decreasing values of $c_A^{L_A}$, the state of the system is represented by the curves marked as I:W. The two sets of curves merge at values of $c_A^{L_A}$ which are larger than the value at which intrusion occurs, which is the limit of stability of the Cassie state, and for values of $c_A^{L_A}$ which are smaller than the value at which the Wenzel state becomes unstable.

In Fig. 10 we show hysteresis loops for $\epsilon_B/\epsilon_A = 2.1$ ($\theta_{AB} \approx 57^\circ$) and $\epsilon_B/\epsilon_A = 2.0$ ($\theta_{AB} \approx 59^\circ$), in terms of the averaged number densities of the B particles only. For $\theta_{AB} \approx 57^\circ$

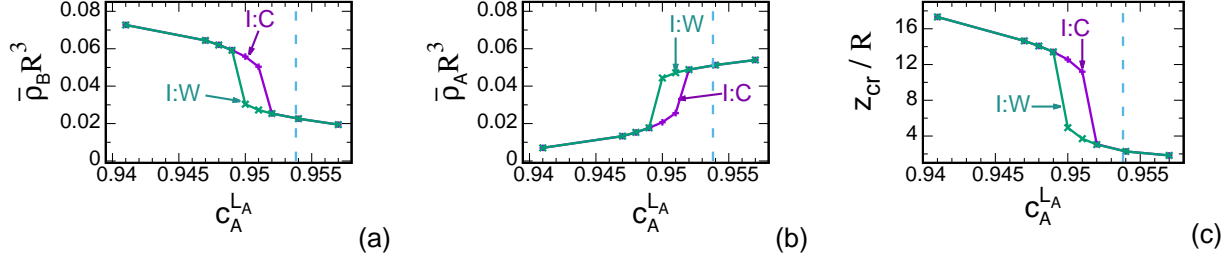


FIG. 9. Averaged number densities of the B particles (panel (a)) and of the A particles (panel (b)) inside the pit, and the position z_{cr} of the L_A-L_B interface (panel (c)) as the concentration c_A^{LA} of the A particles in the ambient liquid is varied along path P_1 in Fig. 2. The results depend on whether the iterations are initialized in a Cassie type state (I:C) or in a Wenzel type state (I:W). The ratio of the wall- A to the wall- B interaction strengths correspond to a contact angle $\theta_{AB} \approx 30^\circ$. The width of the pit is $20R = 10\sigma$ and the depth is $16R = 8\sigma$. The remaining parameters are the same as in all other figures. The position of the Cassie to Wenzel transition, as expected from the macroscopic theory, is indicated by the dashed line.

a wide but still closed hysteresis loop is observed. However, for ($\theta_{AB} \approx 59^\circ$) the loop does not close for values of c_A^{LA} above those of bulk coexistence. In order to obtain a closed hysteresis loop also for ($\theta_{AB} = 59^\circ$) one would have to lower c_A^{LA} to values for which L_A is, however, only metastable in the bulk. The widening of the hysteresis loops, which is observed as θ_{AB} increases, and the observation of an open hysteresis loop for $\theta_{AB} \approx 59^\circ$, can be understood in terms of a mechanism related to corner wetting by the lubricant liquid L_B . In order to move from the Wenzel to the Cassie state, an L_A-L_B interface spanning the pit must be created, which then can be raised up to the pit entrance. The spanning interface can be created by forming 'drops' of the lubricant liquid L_B in the four

corners at the bottom of the pit. If these corner drops can grow until they merge, the spanning interface is created. According to macroscopic capillary theory, for a contact angle $\theta_{AB} = \arccos(1/\sqrt{3}) \approx 54.7^\circ$ and at bulk L_A – L_B coexistence, the shift of a planar L_A – L_B interface formed at a corner is possible without changing the free energy. For larger contact angles θ_{AB} a growth of the corner drops is not possible without surmounting a free energy barrier at bulk liquid–liquid coexistence and in the thermodynamic region of a stable liquid L_A . For contact angles $\theta_{AB} < 54.7^\circ$ the barrierless growth of the corner drops is always possible at bulk liquid–liquid coexistence. At concentrations $c_A^{L_A}$ somewhat above the coexistence value these drops can grow, without barrier, up to the size for which they merge. According to the macroscopic theory, the concentration up to which this mechanism works, increases with decreasing contact angle θ_{AB} and also with a decreasing width of the pit. In our microscopic calculations the transition from a closed hysteresis loop to an open hysteresis loop is observed in the interval $57^\circ < \theta_{AB} < 59^\circ$, i.e., it is shifted to a contact angle somewhat above the value of 54.7° predicted by the macroscopic theory. The mechanism discussed above is very closely related to the one discussed in detail in Ref. [18], for the standard Wenzel to Cassie transition in a liquid–vapor system.

The conditions for intrusion of the ambient liquid into the pit filled by the lubricant, as determined from the microscopic theory, qualitatively agree with the macroscopic predictions for capillary coexistence. At capillary coexistence, the L_A – L_B interface can be moved ‘up’

and 'down' along the capillary (i.e., along the 'vertical' walls of the pit) without changing the free energy (neglecting gravity). This condition is equivalent to a force balance between the force resulting from the pressure difference between the two liquids and the net capillary force due to the difference between the interfacial tensions σ_{sA} and σ_{sB} . Within a macroscopic description the same force balance applies also at the pit entrance through which the liquid intrudes; the liquid–liquid interface is already present. The microscopic computations show that the intrusion transition occurs somewhat closer to bulk coexistence than predicted by the macroscopic theory. We would like to emphasize again, that although the pressure of the ambient liquid L_A decreases as one moves away from coexistence along path P_1 (see Fig. 4), en route, at a certain value of the L_A pressure, the liquid L_A intrudes, because the pressure in the liquid L_B decreases even more so, as a result of changes in the composition and density of the liquid L_B , which are required in order to maintain chemical equilibrium.

2. *Effect of the pit dimensions*

In order to study the influence of the pit dimensions on the intrusion of the ambient liquid into the pit (Cassie to Wenzel transition) and on the reverse process, i.e., the recovery of the Cassie state from the Wenzel state, we first carried out computations for pits with a reduced width of $w = 7\sigma$, but with the same depth $D = 8\sigma$ as the one studied above. In Fig. 11 we show hysteresis loops for two selected contact angles $\theta_{AB} \approx 30^\circ$ and $\theta_{AB} \approx 59^\circ$ and compare

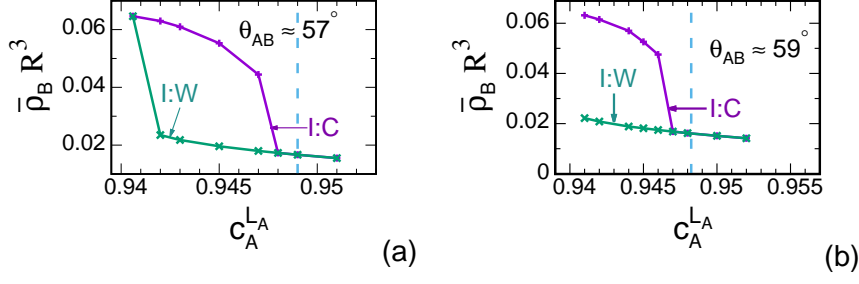


FIG. 10. Averaged number densities of the B particles inside the pit as a function of c_A^{LA} along path P_1 in Fig. 2. The results depend on whether the numerical iterations are initialized in a Cassie type state (I:C) or in a Wenzel type state (I:W). The ratio of the wall- A to the wall- B interaction strength corresponds to contact angles $\theta_{AB} \approx 57^\circ$ (panel (a)) and $\theta_{AB} \approx 59^\circ$ (panel (b)). The width of the pit is $w = 20R = 10\sigma$ and the depth is $D = 16R = 8\sigma$. The remaining parameters are the same as in all other figures. The position of the Cassie to Wenzel transition, as expected from the macroscopic theory, is indicated by the dashed line.

them with the corresponding ones obtained for the wider pits ($w = 10\sigma$, see Fig. 10), which have been discussed above. As can be seen, the intrusion transition (curves I:C) is shifted to larger concentrations c_A^{LA} , i.e., farther away from bulk coexistence, as compared with the concentrations predicted by macroscopic theory (Eq. (2.15)). Like in the case of the wider pits, the concentration c_A^{LA} , at which the intrusion transition occurs, is somewhat closer to the one at bulk coexistence, than the macroscopic theory predicts. The deviation of the macroscopic prediction from the result of the DFT computations is somewhat larger for the narrower pits than it is for the wider pits. Comparing the hysteresis loops obtained for the pits with a width of $w = 7\sigma$ and the ones obtained for the wider pits ($w = 10\sigma$), a striking

difference is found. For $\theta_{AB} \approx 59^\circ$ the hysteresis becomes a closed loop for the narrow pit ($w = 7\sigma$), whereas an 'open' loop is found for the wider pit ($w = 10\sigma$); for $\theta_{AB} \approx 30^\circ$ the hysteresis becomes very slender for the narrow pit ($w = 7\sigma$). For the narrow pit ($w = 7\sigma$, $D = 8\sigma$), the hysteresis remains a closed loop up to the contact angle $\theta_{AB} \approx 70^\circ$ and turns into an 'open' loop within the interval $70^\circ < \theta_{AB} < 73^\circ$. Thus the range of contact angles θ_{AB} within which the recovery of the Cassie state (i.e., refilling of the pit with the lubricant) is possible, drastically extends into the regime of rather large contact angles. According to the macroscopic theory, a barrier-free transition from the Wenzel state to the Cassie state is not possible for contact angles above $\theta_{AB} \approx 54.7^\circ$ in the thermodynamic regime in which the liquid L_A is stable. Apparently, due to various confinement effects, there is an enhancement of the wettability of the walls by the liquid L_B near the corners, as compared to what is expected on the basis of the contact angle θ_{AB} . (We note that θ_{AB} is defined for a macroscopically extended planar wall.) The sizes of the corner-droplets, as they merge to form a spanning L_A - L_B interface, are very small for narrow pits and thus are strongly affected by the confinement effects. They behave as if they are in contact with a more wettable wall, which favors the destabilization of the Wenzel state and the transformation into the Cassie state via the corner wetting mechanism. These considerations explain why the contact angle θ_{AB} , at which the transition between a closed loop to an 'open' loop hysteresis occurs, shifts to larger values upon decreasing the width of the pits. This finding is very similar to what

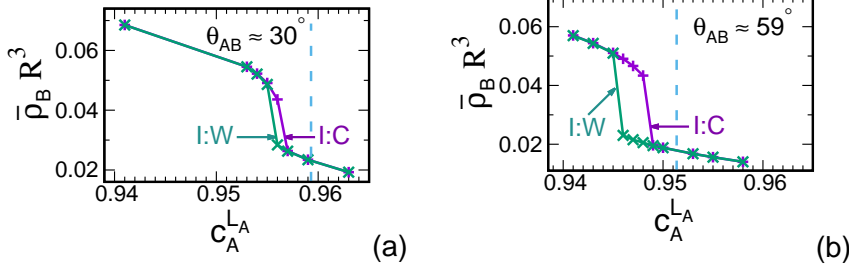


FIG. 11. Averaged number densities of the B particles inside the pit as a function of $c_A^{L_A}$ along path P_1 in Fig. 2. The results depend on whether the iterations are initialized in a Cassie type state (I:C) or in a Wenzel type state (I:W). The ratio of the wall- A to the wall- B interaction strengths corresponds to the contact angles $\theta_{AB} \approx 30^\circ$ (panel (a)) and $\theta_{AB} \approx 59^\circ$ (panel (b)). The width of the pit is $w = 14R = 7\sigma$ the depth is $D = 16R = 8\sigma$. The remaining parameters are the same as in all other figures. The position of the Cassie to Wenzel transition expected from the macroscopic theory is indicated by the dashed line.

is found for the standard Wenzel to Cassie transition for a liquid-vapor system [18]. There the contact angle, above which the Wenzel state may become unstable, shifts to smaller values as compared to the macroscopic predictions for wedge drying. This shift increases upon decreasing the width of the pit.

In addition to the examples discussed in detail above, we have carried out a number of further DFT studies for various contact angles θ_{AB} (i.e., various ratios ϵ_B/ϵ_A) for pits with dimensions $w = 7\sigma$ and $D = 8\sigma$. The key results of these systems are compiled in Table I and can be compared with the corresponding ones for wider pits ($w = 10\sigma$ and $D = 8\sigma$) listed in the same table.

In a further series of DFT computations, we have reduced the depth from $D = 8\sigma$ to $D = 6\sigma$, keeping the width fixed at $w = 7\sigma$. As an example, in Fig. 12 we show, for the contact angle $\theta_{AB} \approx 30^\circ$, the averaged number density of the B particles inside the pit as the concentration c_A^{LA} in the ambient liquid is varied at constant packing fraction (path P_1 in Fig. 2). The hysteresis, still present for the deeper pit, disappears completely for the shallower pit, and the intrusion transition is slightly shifted to a smaller concentration c_A^{LA} . Macroscopic capillarity theory does not and cannot predict a dependence of the intrusion transition on the depth of the pit, but actually there is one. For shallow pits the features near the pit entrance, which are responsible for the intrusion behavior, are affected by the presence of the bottom of the pit. Vice versa, the characteristics of the corners at the bottom of the pit are affected by the presence of the pit entrance. We have carried out a number of further DFT studies for various contact angles θ_{AB} (i.e., various ratios ϵ_B/ϵ_A) for these pit dimensions ($w = 7\sigma$ and $D = 6\sigma$). The corresponding key results are also compiled in Table I.

Repeating the same type of computations for a series of packing fractions of the ambient liquid, for each contact angle θ_{AB} and each pit width w (and depth D) one can determine two spinodal lines running 'parallel' to the bulk liquid–liquid coexistence line (see the sketch in Fig. 13). One of these spinodal lines corresponds to the intrusion transition (i.e., the limit of stability of the Cassie state). The second spinodal line describes the stability limit of the

TABLE I. Macroscopic and DFT results for intrusion as a function of $c_A^{L_A}$, at fixed total packing fraction $\eta^{L_A} = 0.4069093$, for various contact angles θ_{AB} , and for three sets of geometric parameters. The macroscopic prediction for the concentration $c_A^{L_A}$, at which the Cassie to Wenzel transition occurs, is identified with the macroscopic prediction of liquid-liquid capillary coexistence. For complete wetting, i.e., $\theta_{AB} = 0^\circ$ a lower bound for this concentration is given, which follows from Eq. (2.15) with $\cos \theta_{AB} = 1$. (In the bulk, L_A and L_B coexist at $c_A^{L_A} \approx 0.941$.) For the reverse transition (I:W) a detailed macroscopic theory is not available. In this regime the transitions may be gradual within a wide concentration interval. In these cases the interval given in the table contains about 70% of the changes in the average number densities inside the pit, the rest of the changes is roughly equally distributed between the regimes in which the concentrations are either below or above the given interval. In the other cases there is a jump from the Cassie state at the lower concentration value of the given interval to the Wenzel state at the next higher concentration, which is varied in steps of 0.001.

ϵ_B/ϵ_A	θ_{AB}	macroscopic $c_A^{L_A}$ at transition	DFT results		
			$c_A^{L_A}$ interval of transition		hysteresis
		I:C	I:C	I:W	
$w = 10\sigma, D = 8\sigma$ (Fig. 10)					
4.0	0°	0.9561	0.954 - 0.967	0.954 - 0.967	no
3.5	0°	0.9561	0.953 - 0.956	0.953 - 0.956	no
3.4	0°	0.9561	0.955 - 0.956	0.955 - 0.956	no
3.2	12°	0.9558	0.954 - 0.955	0.954 - 0.955	no
3.1	18°	0.9553	0.953 - 0.954	0.952 - 0.953	yes
2.8	30°	0.9530	0.951 - 0.952	0.948 - 0.949	yes
2.2	54°	0.9498	0.947 - 0.948	0.942 - 0.943	yes
2.1	57°	0.9490	0.947 - 0.948	0.941 - 0.942	yes
2.0	59°	0.9480	0.946 - 0.947	—	'open loop'
$w = 7\sigma, D = 8\sigma$ (Fig. 11)					
4.0	0°	0.9626	0.963 - 0.970	0.963 - 0.970	no
3.4	0°	0.9626	0.960 - 0.962	0.960 - 0.962	no
3.3	0°	0.9626	0.959 - 0.960	0.959 - 0.960	no
3.0	23°	0.9608	0.957 - 0.958	0.957 - 0.958	no
2.9	26°	0.9601	0.956 - 0.957	0.956 - 0.957	no
2.8	30°	0.9593	0.956 - 0.957	0.955 - 0.956	yes
2.0	59°	0.9510	0.948 - 0.949	0.944 - 0.945	yes
$w = 7\sigma, D = 6\sigma$ (Fig. 12)					
4.0	0°	0.9626	0.963 - 0.970	0.963 - 0.970	no
3.3	0°	0.9626	0.958 - 0.960	0.958 - 0.960	no
3.2	12°	0.9557	0.958 - 0.960	0.958 - 0.960	no
2.8	30°	0.9593	0.954 - 0.955	0.954 - 0.955	no
2.5	43°	0.9560	0.951 - 0.952	0.951 - 0.952	no
2.3	51°	0.9540	0.949 - 0.950	0.948 - 0.949	yes
2.0	59°	0.9510	0.946 - 0.947	0.943 - 0.944	yes

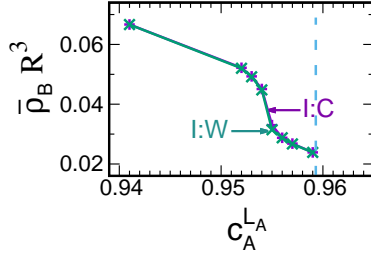


FIG. 12. Averaged number density of the B particles inside the pit as a function of $c_A^{L_A}$ along path P_1 in Fig. 2. The ratio of the wall- A to the wall- B interaction strengths corresponds to a contact angle $\theta_{AB} \approx 30^\circ$. Here, the results do not depend on whether the iterations are initialized in a Cassie type state (I:C) or in a Wenzel type state (I:W). The width of the pit is $w = 14R = 7\sigma$ and the depth is $D = 12R = 6\sigma$. The remaining parameters are the same as the ones in all other figures. The position of the Cassie to Wenzel transition, as expected from the macroscopic theory, is indicated by the dashed line.

Wenzel state. It characterizes the reverse transition, called 'extrusion transition', i.e., the Wenzel to Cassie transition, at which a pit filled with the liquid L_A refills with the liquid L_B . For contact angles θ_{AB} below a certain threshold value, which depends on the width of the pit, this second spinodal line might be located between the bulk liquid-liquid coexistence line and the spinodal line for intrusion (see Fig. 13 (a)). For small contact angles, in which case no hysteresis is observed, the line marking this stability limit coincides with the one locating the intrusion transition. For contact angles above the limiting one the spinodal line for extrusion does no longer lie within the domain of the stable bulk liquid L_A (see Fig. 13 (b)), which corresponds to the 'open loop' hysteresis mentioned above. For concentrations

c_A^{LA} of the ambient liquid below the one of capillary liquid–liquid coexistence, but above the one at the extrusion spinodal, the Wenzel state remains metastable. (For deep pits the capillary liquid–liquid coexistence is at concentrations c_A^{LA} very close to and slightly below the one of the intrusion spinodal.) We refrain from performing such extensive computations. Instead we have carried out a few DFT calculations at constant concentration c_A^{LA} of the ambient liquid, changing the packing fraction (i.e., the pressure) along path P_2 in Fig. 2. The purpose of these calculations is twofold. First, we want to corroborate the above picture and to find the spinodal lines at much higher packing fractions. Second, we want to check whether the picture developed so far is complete, or whether an unexpected dependence on the path taken in the phase diagram is observed.

B. Cassie–Wenzel and Wenzel–Cassie transition at fixed concentration

In this subsection, we present results of DFT calculations carried out at constant concentration $c_A^{LA} = 0.941$ in the ambient liquid. The packing fraction in the ambient liquid is increased in steps from $\eta^{LA} = 0.40696$, along path P_2 in Fig. 2, towards the one at which liquid–liquid coexistence occurs in the bulk, at the chosen concentration. We follow the evolution of the (meta)stable states along this path. As before we have initialized the iterative determination of the number densities in a Cassie type configuration (I:C) as well as in a Wenzel type configuration (I:W). We have studied pits with the same geometric

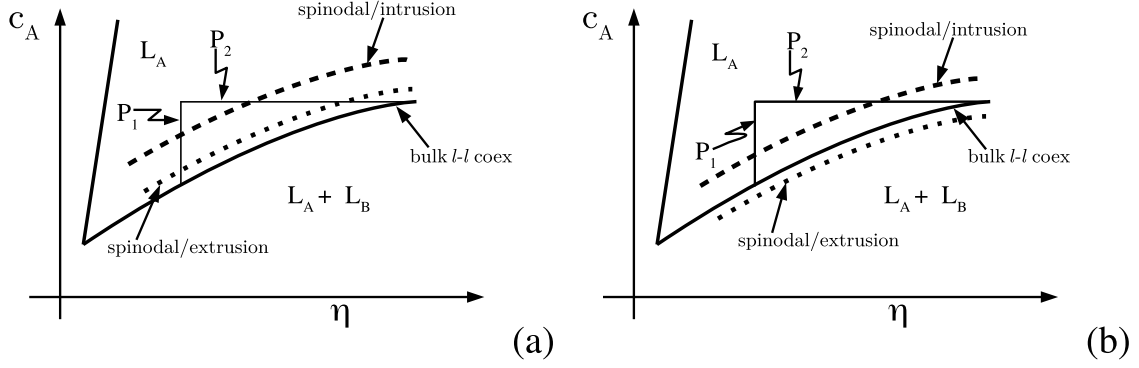


FIG. 13. Sketch of the relative locations of the spinodal line for the intrusion transition (dashed line), the spinodal line for the reverse transition, i.e., the 'extrusion transition' (dotted curve), and of the bulk liquid-liquid coexistence line (full line). Panel (a) [(b)] holds for contact angles θ_{AB} below [above] a limiting contact angle, which is $\theta_{AB} \approx 54.7^\circ$ for macroscopic pits. For nanoscopic pits, this limiting contact angle depends on the width of the pit. The thin lines correspond to the thermodynamic paths 1 and 2, respectively.

parameters ($w = 10\sigma$, $D = 8\sigma$), ($w = 7\sigma$, $D = 8\sigma$), and ($w = 7\sigma$, $D = 6\sigma$) as considered in the previous subsection. We have also carried out computations for various ratios ϵ_B/ϵ_A of the interactions between the B and A particles, respectively, with the wall particles. Instead of specifying this ratio, we use the contact angle θ_{AB} at the particular packing fraction $\eta^{LA} = 0.40696$. This was suitable for the purpose of the analyses in the previous subsection. Since the contact angle depends on the packing fraction and because the transitions to be studied occur at high packing fractions, for a quantitative comparison with the macroscopic theory it might be better to determine the contact angle for an appropriate packing fraction. However, these details are not relevant for our purpose and, by always referring to the

same packing fraction $\eta^{LA} = 0.40696$, equal contact angles correspond to equal ratios ϵ_B/ϵ_A , which is beneficial from another point of view.

Based on the picture developed in the previous section, we expect the following evolution of configurations upon moving along path P_2 in Fig. 2. At $(c_A^{LA} = 0.941, \eta^{LA} = 0.40696)$ one knows that, whether the iteration scheme is started in the Cassie state (I:C) or in the Wenzel state (I:W), the Wenzel state as the equilibrium one will be eventually reached. Increasing the packing fraction upon moving along path P_2 , the same behavior will be observed until the spinodal line marking the intrusion transition (i.e., the limit of stability of the Cassie state) is crossed (see Fig. 13). Beyond this crossing, the Cassie state remains stable for the I:C initial condition. The occurrence of the phenomena, which follow from choosing the I:W initial condition, depends on the contact angle and on the geometric parameters. For small contact angles the resulting equilibrium state is the same for both initial conditions, I:C and I:W. For higher contact angles one finds that the Wenzel state remains (meta)stable (for the I:W computations) up to a packing fraction at which the second spinodal, marking the limit of (meta)stability of the Wenzel state, is crossed (see Fig. 13 (a)). Beyond that, the Cassie state is found to be independent of whether I:C or I:W initial conditions are used. For even larger contact angles the Wenzel state remains (meta)stable up to the bulk liquid–liquid coexistence line (see Fig. 13 (b)).

The DFT computations fully confirm the expected behavior. No unexpected features of

the system emerge by following path P_2 instead of path P_1 . For example, in Fig. 14 the averaged number densities inside a wide pit ($w = 10\sigma$, $D = 8\sigma$) are shown as function of the packing fraction in the ambient liquid for a complete wetting situation ($\epsilon_B/\epsilon_A = 4.0$) and for the contact angles $\theta_{AB} \approx 30^\circ$ and $\theta_{AB} \approx 59^\circ$. In the first case one finds, without any hysteresis, a smooth transition to the Cassie state as the packing fraction is increased. In the second case, upon increasing the packing fraction, a transition to the Cassie state first appears within the I:C computations. In the I:W computations the transition occurs at a slightly higher packing fraction. For the contact angle $\theta_{AB} \approx 59^\circ$ it seems as if one encounters again an 'open loop' hysteresis; currently this is only a hypothesis because we do not have results for total packing fractions up to the bulk liquid-liquid coexistence at $\eta^{LA} = 0.46898504$ for the chosen concentration $c_A^{LA} = 0.967$. At these high total packing fractions strongly structured and peaked number densities form inside the pit. It becomes difficult to reach convergence in the numerical iterations. This particular phenomenon also deserves a study of its own.

One also finds, in line with the insights gained in the previous section, that the intrusion and extrusion transitions are shifted to lower packing fractions if the width w of the pit is decreased (see Fig. 15 (a)); the spinodal lines are shifted further away from the bulk coexistence curve as w is decreased. These shifts can be inferred also from Table II. In addition, the data presented in this table reveal how an open loop hysteresis transforms into

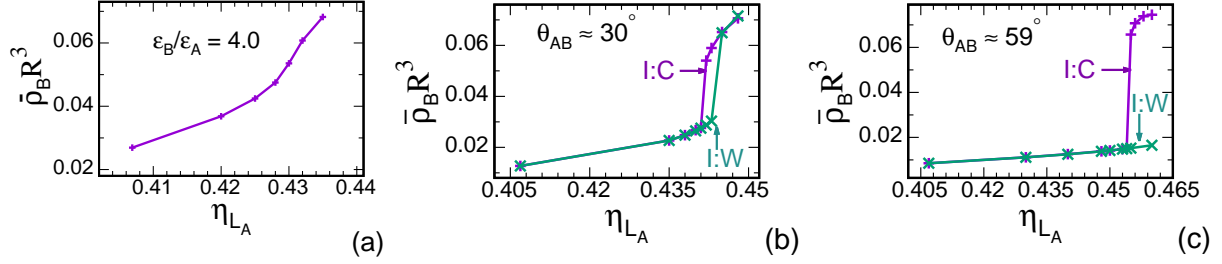


FIG. 14. Averaged number densities of B particles inside the pit, obtained from DFT, as a function of η^{LA} for $w = 10\sigma$, $D = 8\sigma$, and $c_A^{LA} = 0.967$. The ratio ϵ_B/ϵ_A of the wall- B to the wall- A interaction strengths corresponds to complete wetting $\theta_{AB} = 0^\circ$ ($\epsilon_B/\epsilon_A = 4.0$, panel (a); the curves I:C and I:W coincide), to a contact angle $\theta_{AB} \approx 30^\circ$ (panel (b)), and to a contact angle $\theta_{AB} \approx 59^\circ$ (panel (c)).

a closed loop hysteresis as w is reduced from 10σ to 7σ , with otherwise identical system parameters. Figure 15 (b) demonstrates that shallow pits lead to narrow hysteresis loops.

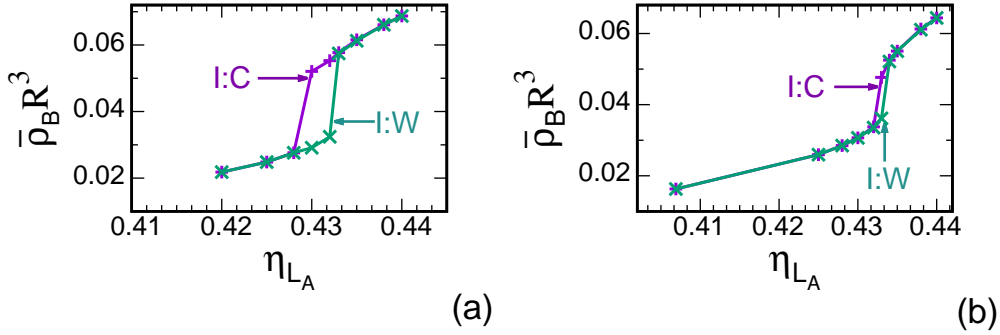


FIG. 15. Averaged number densities of the B particles inside the pit, calculated by using DFT, as a function of η^{LA} at $c_A^{LA} = 0.967$. The ratio ϵ_B/ϵ_A of the wall- A to the wall- B interaction strengths corresponds to $\theta_{AB} \approx 30^\circ$. Two sets of geometric parameters are considered: $w = 7\sigma$ and $D = 8\sigma$ for panel (a), $w = 7\sigma$ and $D = 6\sigma$ for panel (b).

It is interesting to note, that in the present case *reducing* the packing fraction (i.e., reduc-

TABLE II. DFT results for the Cassie to Wenzel and the Wenzel to Cassie transitions at fixed concentration $c_A^{LA} = 0.967$ as a function of the total packing fraction η^{LA} for various contact angles θ_{AB} and three sets of geometric parameters w and D . The contact angles given in the table correspond to liquid–liquid coexistence at a total packing fraction $\eta^{LA} = 0.4069093$ as in Table I. In the complete wetting regime the transitions might exhibit a gradual behavior with about 70% of the changes within the given interval of total packing fractions. For the intervals of width 0.001, corresponding to the steps in which η^{LA} is changed, the system is in the Wenzel state at total packing fractions at and below the lower value of the given interval, and it is in the Cassie state at and above the upper value of the interval.

ϵ_B/ϵ_A	θ_{AB}	η^{LA} interval of transition		hysteresis
		I:C	I:W	
$w = 10\sigma, D = 8\sigma$ (Fig. 14)				
4.0	0°	0.420 - 0.432	0.420 - 0.432	no
3.6	0°	0.430 - 0.436	0.430 - 0.436	no
3.5	0°	0.434 - 0.435	0.434 - 0.435	no
3.4	0°	0.435 - 0.436	0.435 - 0.436	no
3.2	12°	0.436 - 0.437	0.437 - 0.438	yes
2.8	30°	0.440 - 0.441	0.444 - 0.445	yes
2.2	54°	0.449 - 0.450	0.461 - 0.462	yes
2.0	59°	0.454 - 0.455	—	'open loop'
$w = 7\sigma, D = 8\sigma$ (Fig. 15 (a))				
4.0	0°	0.410 - 0.415	0.410 - 0.415	no
3.7	0°	0.410 - 0.417	0.410 - 0.417	no
3.4	0°	0.418 - 0.422	0.418 - 0.422	no
3.3	0°	0.422 - 0.423	0.422 - 0.423	no
3.1	18°	0.425 - 0.426	0.425 - 0.426	no
3.0	23°	0.426 - 0.427	0.427 - 0.428	yes
2.8	30°	0.429 - 0.430	0.432 - 0.433	yes
2.0	59°	0.445 - 0.446	0.461 - 0.462	yes
$w = 7\sigma, D = 6\sigma$ (Fig. 15 (b))				
4.0	0°	0.410 - 0.420	0.410 - 0.420	no
3.3	0°	0.422 - 0.430	0.422 - 0.430	no
3.0	23°	0.425 - 0.431	0.425 - 0.431	no
2.9	26°	0.431 - 0.432	0.431 - 0.432	no
2.8	30°	0.432 - 0.433	0.433 - 0.434	yes
2.0	59°	0.447 - 0.448	0.460 - 0.461	yes

ing the pressure) triggers the Cassie to Wenzel transition. In the well known liquid–vapor systems, the Cassie to Wenzel transition is induced by *increasing* the pressure. However, in both cases the transition occurs upon moving away from bulk coexistence.

IV. SUMMARY, CONCLUSIONS, AND OUTLOOK

By using microscopic density functional theory, we have studied the intrusion transition of an ambient liquid into cavities which are filled with a lubricant liquid. We have considered the case that the lubricant liquid adsorbs at the walls of the cavities more strongly than the ambient liquid does. In order to model the ambient and the lubricant liquids, a binary liquid mixture composed of A and B particles is investigated which decomposes into an A rich liquid, (i.e., the ambient liquid), and a B rich liquid, (i.e., the lubricant liquid). The B particles are taken as the ones which are attracted more strongly by the walls. The cavities are modeled as square pits of width w and depth D (Fig. 1). The intrusion transition is triggered by changing the composition of the ambient liquid (see Table I and Figs. 7 and 9–12) or its total packing fraction (i.e., the pressure, see Table II and Figs. 14 and 15). However, these parameters are constrained to that region of the bulk phase diagram where the ambient liquid is stable. We have also studied the reverse process in which a pit filled with the ambient liquid undergoes a transition back to a state in which it is filled with the lubricant liquid. Also this transition is triggered by varying the composition or the total

packing fraction of the ambient liquid. Both transitions have been studied for different sizes of the cavities and for various chemical compositions of the walls (giving rise to distinct substrate potentials). In our studies we have considered stable or metastable equilibria, which implies that the composition and the total packing fraction of the lubricant liquid confined in the pits adjust until mechanical and chemical equilibrium is reached.

In order to compare the results of the microscopic computations with the predictions of the macroscopic capillarity model (see Sect. II E), the relative strength of the interaction between the A and the B particles, respectively, and the wall is characterized in terms of the contact angle θ_{AB} formed by the liquid–liquid interface between the two coexisting fluid phases and a planar wall, which is composed of a freely chosen material. The intrusion transition is located in that region of the bulk phase diagram where the ambient liquid is stable in the bulk. Its thermodynamic location qualitatively follows the shift (away from the bulk liquid–liquid coexistence line) predicted by the macroscopic capillarity model with respect to its dependence on the contact angle θ_{AB} and the width of the pit. Quantitatively, the transition found within the microscopic calculations occurs somewhat closer to the bulk liquid–liquid coexistence than predicted by the macroscopic capillarity model (see Figs. 9 and 10 and Table I). The quantitative discrepancies become larger for narrower cavities (compare Figs. 10 and 11). In cases in which the wall is completely wetted by the lubricant liquid ($\theta_{AB} = 0$) the reverse transition follows the same path as for intrusion, i.e., there is

no hysteresis (see Fig. 7). In these cases the transition is rather smooth. Also for small but nonzero contact angles there is no hysteresis, but the transition can be rather sharp. For larger contact angles, one has to move closer to the bulk liquid–liquid coexistence line, as compared to the intrusion transition, in order to trigger the inverse transition from a pit filled with ambient liquid to one filled with the lubricant liquid. In these cases the intrusion transition as well as the reverse transition occur abruptly. For large contact angles the reverse transition may not be found within the regime in which the bulk of the ambient liquid is stable (see Fig. 10 (b)). The contact angle θ_{AB} , above which the reverse transition is not found, depends on the width (and to a certain extent also on the depth) of the pit. For a small width the reverse transition is observed up to quite high contact angles (up to $\theta_{AB} \approx 73^\circ$ for a width of $w = 7\sigma$ and a depth of $D = 8\sigma$). We can associate the reverse transition with a mechanism, which is related to wetting by the lubricant of the corners at the bottom of the pits. A spontaneous reverse transition occurs once the individual ‘droplets’ of lubricant forming at the corners are large enough to merge, which creates a liquid–liquid interface spanning the whole pit. For the geometry studied, according to the macroscopic theory, this mechanism is only possible if $\theta_{AB} < 54.7^\circ$, within the regime in which the ambient liquid is stable in the bulk. However, nanoscale effects shift the contact angle, up to which the reverse transition occurs, to much higher values. This shift becomes more pronounced for smaller widths of the pit. For narrower pits the merging lubricant

'droplets', which are localized at the corners of the bottom of the pits, are small and thus they are more strongly affected by nanoscale effects near the corners than the larger merging droplets in the wider pits. Nanoscale effects originate, for instance, from the extended range of the fluid–wall and the fluid–fluid interactions as well as from density oscillations induced by the walls.

For a nonzero contact angle θ_{AB} , the transitions discussed here typically occur at a spinodal marking the limit of stability of a metastable state. In the case of the intrusion transition – as the thermodynamic conditions for the ambient liquid are gradually shifted away from those for liquid–liquid coexistence in the bulk – the state, in which the pit is filled with lubricant, becomes a metastable state before the intrusion transition occurs. In order to reach the stable state, in which the pit is indeed filled with the ambient liquid, a free energy barrier has to be surmounted. The liquid–liquid interface has to be pushed down to the bottom of the pit, which costs free energy. Only after the liquid–liquid and the lubricant–wall interfaces have disappeared and are replaced by an ambient-liquid – wall interface, the free energy is lowered below the one of the metastable state. In the case of the reverse transition, a pit filled with the ambient liquid, will remain metastable until the lubricant 'droplets', forming at the corners of the pit floor, can merge spontaneously. Thermally assisted barrier crossing can become relevant already slightly off the spinodals. Our studies also contribute to an understanding of these processes.

There are similarities between the Cassie to Wenzel and the Wenzel to Cassie transitions in fluid–vapor systems and the intrusion and reverse transitions in a liquid–liquid system studied here. However, there are also differences. For instance, in fluid–vapor systems intrusion of liquid may be induced by increasing the pressure in the liquid, whereas in the liquid–liquid system intrusion of ambient liquid may be induced by decreasing the pressure of the ambient liquid. Both cases, however, have in common that moving away from the bulk coexistence line (i.e., liquid–vapor and liquid–liquid coexistence, respectively) leads to intrusion.

In the present studies we have tuned the liquid–liquid interaction parameters such that each of the two coexisting liquids contains a small fraction of the respective minority component. We refrained from analyzing the limit of very low mutual solubility of the two liquids. We expect that the main phenomena remain the same also in that limit.

The picture provided by the present study offers guidelines for designing slippery liquid infused porous surfaces. However, also other applications of porous surfaces might be envisaged, which make use of the possibility to switch forth and back between wetting states in order to switch other associated physical properties of the composite surface.

It would be very interesting, with respect to both basic research and technical applications, to study the dynamics of these transitions. This can be achieved, *inter alia*, by applying dynamic density functional (DDFT, see, e.g., Refs. [73, 74]), kinetic Monte Carlo

simulations (see, e.g., Refs. [\[75–80\]](#)), as well as dissipative particle dynamics, which has been used recently to study the intrusion of a mixed binary fluid into a nanochannel [\[81\]](#).

-
- [1] J. Young, F. Chen, Q. Yang, Y. Fang, J. Huo, J. Zhang, and X. Hou, *Adv. Mat. Interf.* **4**, 1700552 (2017).
 - [2] T. S. Wong, S. H. Kang, S. K. Y. Tang, E. J. Smythe, B. D. Hatton, A. Grinthal, and J. Aizenberg, *Nature* **477**, 443 (2011).
 - [3] J. Genzer and K. Efimenko, *Biofouling* **22**, 339 (2006).
 - [4] S. Nishimoto and B. Bhushan, *RSC Adv.* **3**, 671 (2013).
 - [5] P. Ragesh, V. A. Ganesh, S. V. Nair, and A. S. Nair, *J. Mater. Chem. A* **2**, 14773 (2014).
 - [6] S. Pan, A. K. Kota, J. M. Mabry, and A. Tuteja, *J. Am. Chem. Soc.* **135**, 578 (2013).
 - [7] M. J. Kreder, J. Alvarenga, P. Kim, and J. Aizenberg, *Nat. Rev. Mater.* **1**, 15003 (2016).
 - [8] J. Lv, Y. Song, L. Jiang, and J. Wang, *ACS Nano* **8**, 3152 (2014).
 - [9] J. D. Smith, R. Dhiman, S. Anand, E. Reza-Garduno, R. E. Cohen, G. H. McKinley, and K. K. Varanasi, *Soft Matter* **9**, 1772 (2013).
 - [10] M. K. Fu, I. Arenas, S. Leonardi, M. Hultmark, *J. Fluid Mechanics* **824**, 688 (2017).
 - [11] W. Barthlott and C. Neinhuis, *Planta* **202**, 1 (1997).
 - [12] R. N. Wenzel, *Ind. Eng. Chem.* **28**, 988 (1936).
 - [13] A. B. D. Cassie and S. Baxter, *Trans. Faraday Soc.* **40**, 546 (1944).
 - [14] C. Neinhuis and W. Barthlott, *Ann. Bot.* **79**, 667 (1997).
 - [15] D. Quéré, *Rep. Prog. Phys.* **68**, 2495 (2005).
 - [16] A. Lafuma and D. Quéré, *Nat. Mater.* **2**, 457 (2003).
 - [17] A. Giacomello, L. Schimmele, S. Dietrich, and M. Tasinkevych, *Soft Matter* **12**, 8927 (2016).
 - [18] A. Giacomello, L. Schimmele, S. Dietrich, and M. Tasinkevych, *Soft Matter* **15**, 7462 (2019).
 - [19] D. Quéré, *Ann. Rev. Mater. Res.* **38**, 71 (2008).
 - [20] T. P. N. Nguyen, P. Brunet, Y. Coffinier, and R. Boukherroub, *Langmuir* **26**, 18369 (2010).
 - [21] L. Bocquet and E. A. Lauga, *Nat. Mater.* **10**, 334 (2011).
 - [22] R. Poetes, K. Holtzmann, K. Franze, and U. Steiner, *Phys. Rev. Lett.* **105**, 166104 (2010).
 - [23] T. Verho, C. Bower, P. Andrew, S. Franssila, O. Ikkala, and R. H. A. Ras, *Adv. Mater.* **23**, 673 (2011).
 - [24] M. Reyssat, J. M. Yeomans, and D. Quéré, *Europhys. Lett.* **74**, 299 (2006).
 - [25] T. Deng, K. K. Varanasi, M. Hsu, N. Bhate, C. Keimel, J. Stein, and M. Blohm, *Appl. Phys.*

- Lett. **94**, 133109 (2009).
- [26] H. Bellanger, T. Darmanin, E. T. de Givenchy, and F. Guittard, Chem. Rev. **14**, 2694 (2014).
 - [27] Z. L. Chu and S. Seeger, Chem. Soc. Rev. **43**, 2784 (2014).
 - [28] T. Jiang, Z. G. Guo, and W. M. Liu, J. Mater. Chem. A **3**, 1181 (2015).
 - [29] A. Lafuma and D. Quéré, EPL **96**, 56001 (2011).
 - [30] H. F. Bohn and W. Federle, Proc. Natl. Acad. Sci. USA **101**, 14138 (2004).
 - [31] E. K. Epstein, T. K. Wong, R. A. Belisle, E. M. Boggs, and J. Aizenberg, Proc. Natl. Acad. Sci. USA **109**, 13182 (2012).
 - [32] C. Howell, T. L. Vu, J. J. Lin, S. Kolle, N. Juthani, E. Watson, J. C Weaver, J. Alvarenga, and J. Aizenberg ACS Appl. Mater. Interf. **6**, 13299 (2014).
 - [33] S. Nishioka, M. Tenjimbayashi, K. Manabe, T. Matsubayashi, K. Suwabe, K. Tsukada, and S. Shiratori, RSC Adv. **6**, 47579 (2016).
 - [34] P. Kim, T.-S. Wong, J. Alvarenga, M. J. Kreder, W. E. Adorno-Martinez, and J. Aizenberg, ACS Nano **6**, 6569 (2012).
 - [35] P. W. Wilson, W. Lu, H. Xu, P. Kim, M. J. Kreder, J. Alvarenga, and J. Aizenberg, Phys. Chem. Chem. Phys. **15**, 581 (2013).
 - [36] K. Rykaczewski, S. Anand, S. B. Subramanyam, and K. K. Varanasi, Langmuir **29**, 5230 (2013).
 - [37] K. Rykaczewski, A. T. Paxson, M. Staymates, M. L. Walker, X. Sun, S. Anand, S. Srinivasan, G. H. McKinley, J. Chinn, J. H.J Scott, and K. K. Varanasi, Sci. Rep. **4**, 4158 (2014).
 - [38] K.-C. Park, P. Kim, A. Grinthal, N. He, D. Fox, J. C. Weaver, and J. Aizenberg, Nature **531**, 78 (2016).
 - [39] T. Kajiya, S. Wooh, Y. Lee, K. Char, D. Vollmer and H.-J. Butt, Soft Matter **12**, 9377 (2016).
 - [40] G. H. Zhu, C. Zhang, C. Wang, and N. S. Zacharia, Adv. Mat. Interf. **3**, 1600515 (2016).
 - [41] S. Sunny, N. Vogel, C. Howell, T. L. Vu, and J. Aizenberg, Adv. Funct. Mater. **24**, 6658 (2014).
 - [42] G. H. Zhu, S.-H. Cho, H. Zhang, M. Zhao, and N. S. Zacharia, Langmuir **34**, 4722 (2018).
 - [43] G. H. Zhu, C. Zhang, C. Wang, and N. S. Zacharia, Adv. Mat. Interf. **3**, 1600515 (2016).
 - [44] W. Ma, Y. Higaki, H. Otsuka, and A. Takahara, Chem. Commun. **49**, 597 (2013).
 - [45] P. Wang, D. Zhang, S. Sun, T. Li, and Y. Sun, ACS Appl. Mater. Interf. **9**, 972 (2017).
 - [46] S. Yuan, Z. Li, L. Song, H. Shi, S. Luan, and J. Yin, ACS Appl. Mater. Interf. **8**, 21214 (2016).

- [47] J. Wang, K. Kato, A. P. Blois, and T.-S. Wong, ACS Appl. Mater. Interf. **8**, 8265 (2016).
- [48] S. Nishioka, M. Tenjimbayashi, K. Manabe, T. Matsubayashi, K. Suwabe, K. Tsukada, and S. Shiratori, RSC Adv. **6**, 47579 (2016).
- [49] X. Yao, J. Ju, S. Yang, J. Wang, and L. Jiang, Adv. Mater. **26**, 1895 (2014).
- [50] E. Jenner and B. D’Urso, Appl. Phys. Lett. **103**, 251606 (2013).
- [51] V. Hejazi and M. Nosonovsky, Langmuir **28**, 2173 (2012).
- [52] X. Hou, Y. Hu, A. Grinthal, M. Khan, and J. Aizenberg, Nature **519**, 70 (2015).
- [53] M. Ulbricht, Nature **519**, 41 (2015).
- [54] A. D. Stroock, V. V. Pagay, M. A. Zwieniecki, and N. M. Holbrook, Annu. Rev. Fluid Mech. **46**, 615 (2014).
- [55] W. S. Y. Wong, K. I. Hegner, V. Donadei, L. Hauer, A. Naga, and D. Vollmer, Nano Lett. **20**, 8508 (2020).
- [56] O. Peleg and R. Y. H. Lim, Biol. Chem. **391**, 719 (2010).
- [57] S. L. Singh, L. Schimmele, and S. Dietrich, Phys. Rev. E. **101**, 052115 (2020).
- [58] K. Reijmer, S. Dietrich, and M. Napiórkowski, Phys. Rev. E. **60**, 4027 (1999).
- [59] A. Malijevsky and A. O. Parry, Phys. Rev. Lett. **120**, 135701 (2018).
- [60] A. Malijevsky, Phys. Rev. E **102**, 012804 (2020).
- [61] A. Malijevsky and A. O. Parry, J. Phys.: Condens. Matter **26**, 355003 (2014).
- [62] J. D. Weeks, D. Chandler, and H. C. Andersen, J. Chem. Phys. **54**, 5237 (1971).
- [63] S. L. Singh, L. Schimmele, and S. Dietrich, Phys. Rev. E. **91**, 032405 (2015).
- [64] R. Evans, Adv. Phys. **28**, 143 (1979).
- [65] Y. Singh, Phys. Rep. **207**, 351 (1991).
- [66] R. Roth, R. Evans, A. Lang, and G. Kahl, J. Phys.: Condens. Matter **14**, 12063 (2002).
- [67] P. Tarazona, J.A. Cuesta, and Y. Martínez-Ratón, in *Lecture Notes in Physics* (Springer, Heidelberg, 2008) vol. 753, p. 247.
- [68] Y. Rosenfeld, Phys. Rev. Lett. **63**, 980 (1989).
- [69] Y. Rosenfeld, M. Schmidt, H. Löwen, and P. Tarazona, Phys. Rev. E **55**, 4245 (1997).
- [70] R. Roth, J. Phys.: Condens. Matter **22**, 063102 (2010).
- [71] S. Dietrich, in *Phase Transitions and Critical Phenomena*, edited by C. Domb and J. L. Lebowitz (Academic, London, 1988), Vol. 12, p.1.
- [72] R. Evans and U. Marini Bettolo Marconi, J. Chem. Phys. **86**, 7138 (1987).

- [73] A. J. Archer and R. Evans, J. Chem. Phys. **121**, 4246 (2004).
- [74] M. Rauscher, Dynamic Density Functional Theory (DDFT), in *Encyclopedia of Microfluidics and Nanofluidics*, edited by D. Li (Springer, Boston, MA. (2008)), pp. 693-699.
- [75] M. Apostolopoulou, R. Day, R. Hull, M. Stamatakis,¹ and A. Striolo, J. Chem. Phys. **147**, 134703 (2017).
- [76] K. Binder and D.W. Heermann, Monte Carlo Simulation in Statistical Physics: An Introduction, 6th Edition (Springer, Berlin (2019)).
- [77] M. N. Popescu and S. Dietrich, in *Interface and Transport Dynamics*, Lecture Notes in Computational Science and Engineering, edited by H. Emmerich, B. Nestler, and M. Schreckenberg (Springer, Berlin (2003)), Vol. 32, p. 202.
- [78] M. N. Popescu and S. Dietrich, Phys. Rev. E **69**, 061602 (2004).
- [79] S. Dietrich, M. N. Popescu, and M. Rauscher, J. Phys.: Condens. Matter **17**, S577 (2005).
- [80] M. N. Popescu, S. Dietrich, and G. Oshanin, J. Phys.: Condens. Matter **17**, S4189 (2005).
- [81] T. H. Chakrapani and W. K. den Otter, Langmuir **36**, 12712 (2020).